HYBRID ILLINOIS DEVICE FOR RESEARCH AND APPLICATIONS MATERIAL ANALYSIS TEST-STAND DEVELOPMENT FOR CHARACTERIZATION OF FUSION PLASMA-MATERIAL INTERACTIONS

BY

ANDREW JOHN SHONE

THESIS

Submitted in partial fulfillment of the requirements
for the degree of Master of Science in Nuclear, Plasma, and Radiological Engineering
in the Graduate College of the
University of Illinois Urbana-Champaign, 2021

Urbana, Illinois

Master's Committee:

Research Assistant Professor Daniel Andruczyk, Adviser
Professor David N. Ruzic

ABSTRACT

The Hybrid Illinois Device for Research and Applications (HIDRA) at the University of Illinois at Urbana-Champaign (UIUC) is the only tokamak-stellarator hybrid that is wholly dedicated to the study of material science, mainly research pertaining to fusion plasma facing components (PFCs). HIDRA's long-pulse steady-state stellarator plasmas provide a unique plasma environment to test materials under the harsh conditions they will experience in a fusion device. To realize HIDRA's potential to advance PFC research, the HIDRA-Material Analysis Test-stand (HIDRA-MAT) was designed and fabricated. HIDRA-MAT is an extension of HIDRA with the purpose of exposing materials to HIDRA stellarator plasmas and then performing *in-vacuo* surface characterization. HIDRA's long-pulse plasmas emulate some environmental conditions samples will experience in larger fusion devices, which will help in PFC development by studying the plasma-material interactions. Sample preparation utilizes a high-linear shift mechanism with an attached UHV heater that is rotatable for sample positioning and diagnostic use. A liquid metal droplet injector (LMDI) allows for controlled *in-vacuo* liquid metal droplet creation and application to samples. HIDRA-MAT is equipped with a multitude of diagnostics capable of laser-induced breakdown spectroscopy (LIBS), laser-induced desorption spectroscopy (LIDS), thermal desorption spectroscopy (TDS), and He/D_2 differentiation. Preliminary experimental data demonstrating the functionality of sample motion and rotation, the LMDI, and surface characterization diagnostics (LIBS, LIDS, and TDS), and He/D_2 differentiation is reported. A ±5% error in He/D_2 mixture concentration measurements has been demonstrated and the technique will be used to determine He and D_2 retention in samples after plasma exposure. The LIBS system's development and results are discussed describing how signal quality has been improved. Lithium peaks have been resolved in collected spectra and the implementation of dual-pulsed LIBS is

expected to increase signal strength and allow for the identification of hydrogen and deuterium peaks. The LIBS system's depth profiling capability has also been demonstrated. HIDRA and HIDRA-MAT together present a unique opportunity in the field of fusion PFC research and trailblazes the path for the accumulation of scientific knowledge on liquid metal-PFC-plasma interactions as liquid metals begin to showcase advantageous properties in fusion environments.

ACKNOWLEDGEMENTS

It is rare in life that individual achievements in a person's life are exclusively due to an individual effort. This master's thesis is no exception. I want to thank everyone around me who has supported me in pursuing this master's degree and my future goals.

To begin, thank you to my family, my parents Jim and JoAnne and brothers Joe and Bob, and my girlfriend Kathryn, for their never-ending love and support as I navigate life as a graduate student. They have always reaffirmed the fact that they support me in everything that I do. I cannot be more thankful for that. I must mention that the unrelenting "Shone competitiveness" instilled in me at birth has helped serve as a source of motivation to be the best that I can be in my life and overcome any obstacles graduate school can throw at me.

Next, thank you to my adviser Professor Daniel Andruczyk and second reader, Professor David N. Ruzic, for helping me develop myself as a researcher and being part of my master's committee. Throughout my time here at UIUC, I've always looked up to you both as role models. Your passion for your work and dedication to your students always remind me how happy and grateful I am to be in the NPRE graduate program.

To the postdoctoral researchers Alfonso de Castro and Eitan Barlaz, and all my fellow graduate students, thank you for taking time out of your already stressful schedules to help me in my research. Yes, that includes going out to get "a few" drinks at the bar. Many thanks to all my undergraduate researchers and everyone in the NPRE department that has helped me; without you, completing this master's would not have been possible.

Finally, I'd like to thank all my friends in Chicago and scattered across the country for keeping me sane and reminding me there's always time to relax and get away from the stress. I will also take this moment to say COVID-19 is the worst, and I can't wait for it to be over.

TABLE OF CONTENTS

CHAPTER 1: INTRODUCTION

1.1 Fusion Energy

Fusion energy has long been sought after because of its potential to provide the world with virtually limitless energy. A single working commercial fusion reactor could meet the energy demand from hundreds of thousands of people with little waste and harm to the environment compared to that of energy sources such as fossil fuels and natural gas. A fusion reactor accomplishes this seemly impossible task by forcing atoms to fuse under extreme conditions, much like the Sun.

The underlying scientific principles that lead to fusion in the Sun can produce energy from fusion reactions on Earth. The Sun's gravitational force creates extremely dense plasmas that lead to atomic nuclei fusing in its core. This force cannot be reproduced on Earth, so scientists drive plasma temperatures hotter than the Sun's core. Under these conditions, a deuterium-tritium reaction is possible. Deuterium and tritium are isotopes of hydrogen and, when fused, yield a helium atom and high energy neutron as described in equation 1 [1].

$$D + T \rightarrow {}^{4}He\ [3.56\ MeV] + n\ [14.03\ MeV] \qquad (1)$$

Most of the energetic neutrons escape the fusion vacuum vessel. They are captured by a blanket system that converts the energy to heat used to boil water and spin a turbine, while a fraction is absorbed in the underlying structural components. The alpha particles, being charged, are trapped by the magnetic field and confined and thus continue interact with the plasma by either transferring their energy through collisions with the deuterium and tritium ions to sustain the fusion reaction or, eventually, interacting with the fusion reactor's walls. Discussion on how to achieve

fusion energy has been going on since the 1940s. Still, one thing is certain; developing fusion energy systems is the long term solution for clean, sustainable, and virtually unlimited energy globally.

There are many engineering challenges in constructing a fusion reactor. The plasma-material interactions (PMI) at the device walls have a significant impact on how a fusion reactor is designed. PMI has a direct effect on plasma performance due to impurities being sputtered into the plasma, fuel being implanted into the walls, destruction of reactor walls, and much more. There will always be a need for a vacuum vessel to contain the plasma; thus, there will always be PMI challenges. The following thesis will further discuss PMI, introduce current fusion research devices and technologies used for PMI testing, and provide an in-depth explanation of the design and preliminary results for a unique PMI research tool.

1.2 Hybrid Illinois Device for Research and Applications

The Hybrid Illinois Device for Research and applications (HIDRA), located at the Center for Plasma-Material Interactions (CPMI), is the only tokamak-stellarator hybrid dedicated to the study of PMI for fusion applications. HIDRA, formerly WEGA in Greifswald, Germany, has a major radius $R_0 = 0.72$ m and a minor radius $a = 0.19$ m and is currently being run as a classical stellarator configuration [2]. HIDRA can operate up to ~60 minutes at a low magnetic field (87.5 mT) and tens of minutes in its high magnetic field regime (0.5 T). HIDRA's size and long-pulse plasmas equip it to act as a testbed for PMI research. Though HIDRA cannot reach the heat fluxes seen in larger devices, it can reproduce a similar magnetic field environment and particle flux that will produce relevant PMI edge mechanisms [3]. HIDRA, in combination with PMI diagnostics, can be used to conduct preliminary PMI experiments to provide useful data on plasma-facing

components (PFCs) to aid larger devices in determining what PFCs should be implemented in their experimental campaigns.

1.3 PMI Issues and Stated Objectives

PFCs play a critical role in the development of fusion energy. The numerous underlying mechanisms responsible for PMI have a substantial effect on plasma performance and device design. Testing PFCs in fusion devices proves to be a considerably time-consuming and challenging task. These challenges arise from larger fusion devices (EAST, JET, etc.), having strict experimental schedules that collate data on several fusion energy research disciplines, not just PFCs. Additionally, each device's unique design constraints can impede the feasibility of efficiently testing multiple PFC concepts and restrict experimental campaigns to focus on a single PFC. The development of a practical device dedicated to testing a diverse set of PFC materials in a time-efficient manner would accelerate the development of fusion PFCs.

Fuel and reaction byproduct interactions with the wall have a significant impact on any fusion relevant PFC. Ion implantation leading to fuzz growth [4, 5] and fuel retention [6] have highlighted some issues using solid PFCs. CPMI at the University of Illinois at Urbana-Champaign (UIUC) is one of the leading labs studying the use of liquid metals, specifically lithium, as a PFC in fusion devices [7, 8, 9]. Research at UIUC aims to understand the PMI associated with liquid lithium loops and the engineering required to make them a reality in fusion devices. One such area of PMI being investigated is the retention of D and He in lithium PFCs. The Hybrid Illinois Device for Research and Applications (HIDRA) provides an integral pathway for studies on D and He retention in lithium to be researched in an environment that can imitate some aspects of larger fusion devices.

To efficiently utilize HIDRA for material testing, the HIDRA Material Analysis Test-stand (HIDRA-MAT) is being developed. HIDRA-MAT's design took inspiration from the Material Analysis Particle Probe (MAPP) used on NSTX [10]. Though both devices are used for PFC characterization, HIDRA-MAT differs from MAPP in size and shape due to space constraints around HIDRA and has different characterization capabilities. HIDRA-MAT is an extension to HIDRA capable of surface characterization for various materials before and after plasma exposure. HIDRA-MAT stands apart from other material analysis diagnostics due to its ability to expose liquid metal PFCs to long-pulse stellarator plasmas with periodic in-vacuo surface characterization. A sample can be heated with an ultra-high vacuum (UHV) heater sample stage and have liquid metal applied to it using a liquid metal droplet injector (LMDI). After or in-between plasma exposures, materials can be characterized in-vacuo in the HIDRA-MAT main chamber using laser-induced breakdown spectroscopy (LIBS) and thermal desorption spectroscopy (TDS).

In this report, an in-depth look into HIDRA-MAT's design and the functionality of its components are discussed. The design of the main chamber, sniffer section, LIBS system, LMDI, and transfer arm are explained and shown how each component and section complement each other to meet HIDRA-MAT's design criteria. Preliminary results of lithium droplet application to a heated sample in HIDRA-MAT using the LMDI is shown qualitatively. Results from TDS in HIDRA-MAT show desorption of deuterium from tungsten at temperatures which agree with literature. A quantitative analysis of helium and deuterium differentiation is given yielding good confidence in distinguishing relative helium and deuterium mixture concentrations. The evolution of the LIBS system is described which eventually led to identifying the presence of lithium lines in the LIBS spectra after ablating the surface of a lithiated tungsten foil sample. Lastly, a discussion

on the use of Raman spectroscopy for hydrogen identification in silicon and tungsten samples is included in Appendix A due to it being unsuccessful and further He/D_2 differentiation data is included in Appendix B.

Chapter 2: HIDRA-MAT Overview

2.1 Background

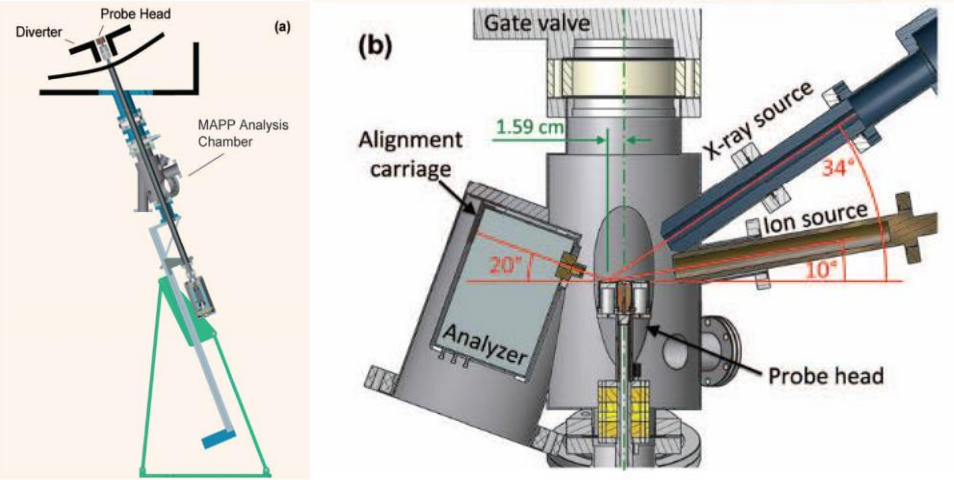

Figure 1. Setup of (a) MAPP on NSTX to expose samples at the divertor region and (b) main chamber of MAPP when samples are being analyzed *[10]*.

The concept of HIDRA-MAT stemmed from the work done on MAPP, shown in figure 1. MAPP was used on NSTX to analyze materials using X-ray photoelectron spectroscopy (XPS), TDS, ion-scattering spectroscopy (ISS), and direct recoil spectroscopy (DRS) directly after plasma exposure. When possible, the design accommodated diagnostics to function within a short time window of a few minutes between shots on NSTX. Each diagnostic component provides surface-sensitive data of the PFCs, including surface chemistry, surface hydrogen detection, and deuterium retention. MAPP's design and experimental data has provided a substantial contribution to PFC research and was used as the benchmark example in the development of HIDRA-MAT.

HIDRA-MAT, similar to MAPP, was fabricated for PFC testing investigating PMI. Though these systems share diagnostic capabilities like TDS, HIDRA-MAT employs diagnostics and sample preparation systems that allow for liquid metal PFC testing and LIBS. Both of these PFC test-stands have unique design constraints and plasma environments. HIDRA's low confinement brings about large particle fluxes to the wall. Samples placed at the plasma edge

during HIDRA's long pulse stellarator plasma paired with HIDRA-MAT's diagnostics will produce preliminary data relevant to developing fusion PFCs. Furthermore, HIDRA-MAT's LMDI enables liquid-metal PFC testing, which has emerged as a necessity as next-generation fusion device design incorporates liquid metal technologies. HIDRA-MAT will test and collect data on a wide variety of PFC materials that will then be used to aid larger devices in deciding on a wide variety of PFC materials that will then be used to aid larger devices in deciding what materials will be used in their experimental campaigns.

2.2 Main Features of HIDRA-MAT

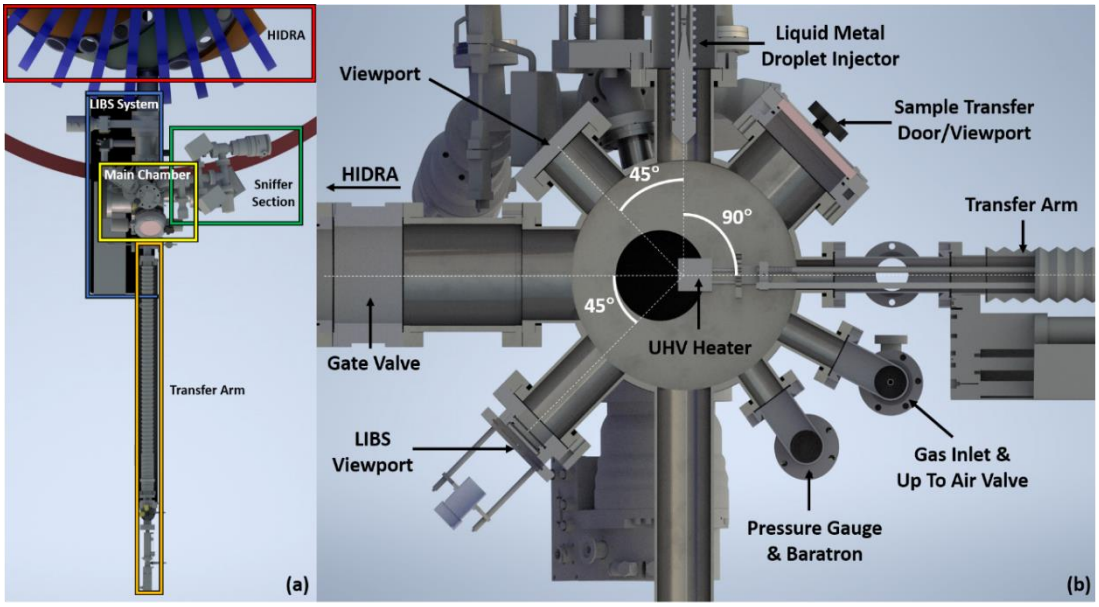

Figure 2. Labeled (a) Top and (b) side views of HIDRA-MAT noting the position of each component and diagnostic in relation to each other.

HIDRA-MAT was designed to conform to HIDRA's space and project budget constraints. HIDRA-MAT is located on a HIDRA A-port between coils 28 and 29 and shown in figure 2. An A-port was chosen because it the largest available port, gives the broadest range of motion for the sample while inside HIDRA, and provides the most space between the vertical field coils for the HIDRA-MAT main chamber and supporting diagnostics to be installed. Secondly, using an A-port means HIDRA-MAT extends outward from HIDRA on a horizontal plane parallel with the floor.

Eliminating the need to work on an angle gave more diagnostic and sample preparation options which are described later in this report. In relation to the other ports on HIDRA, HIDRA-MAT's connection point has B, C, and Z ports next to it currently unused. Cameras and plasma diagnostics could be installed around the sample using these ports to provide more information on the sample exposure conditions. Lastly, HIDRA-MAT's location is on the west end of HIDRA, putting it in the back of NRL 114 and out of sight from the HIDRA control room, adding another layer of safety while the laser system is in use.

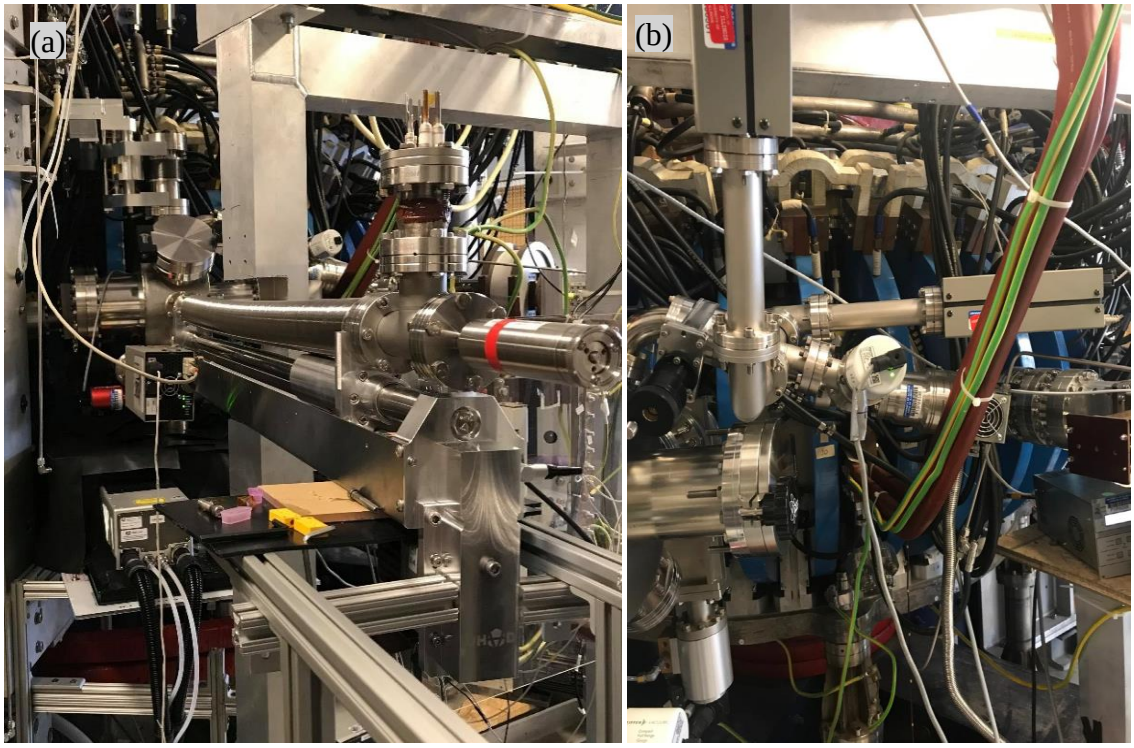

Figure 3. HIDRA-MAT's (a) main chamber, LIBS system, lithium dropper, and transfer arm and (b) sniffer section that contains a dual-RGA system used for TDS and D_2 and He differentiation.

The fabricated final product of HIDRA-MAT is shown in Figures 3a and 3b. An extension piece attached to the A-Port connects to a DN100CF pneumatic gate valve positioned horizontally to the ground and outside of the toroidal field coils. The gate valve allows for maintenance to be done on either HIDRA or HIDRA-MAT while the other is still under vacuum making the two devices independent from each other if need be. The gate valve can also be closed mid-pulse while

HIDRA-MAT diagnostics are running. Closing the gate valve for diagnostic use produces a cleaner environment for testing because of the lower vacuum achieved and the capability to pump background gas into the HIDRA-MAT main chamber without affecting plasma conditions in HIDRA.

A cylindrical vacuum chamber with 12 ports extending out from its top, bottom, and sides acts as the HIDRA-MAT main chamber. The chamber was in a previous experiment and repurposed for HIDRA-MAT. The ports vary in size ranging from DN40CF to DN160CF. Having multiple ports with a line of sight view of the center of the vacuum chamber made it ideal for HIDRA-MAT. The main chamber is compact to fit within the space constraints of HIDRA and versatile to accommodate the different diagnostics and sample preparation systems HIDRA-MAT requires to collect surface sensitive data.

The orientation of the main chamber was dependent on the sample motion between HIDRA-MAT and HIDRA. Two ports in the same plane provide openings for the samples' horizontal movement between the HIDRA-MAT main chamber and the HIDRA vacuum vessel. A high linear shift mechanism is attached to one of these ports and is responsible for the sample's precise automated positioning. The sample head is rotatable and is located on the end of a support rod structure discussed in-depth later on.

The other supporting diagnostics and vacuum components are connected to the main chamber. A DN100CF turbopump backed by a dry, rough pump brings the chamber to a 10^{-7} Torr base pressure. Another gate valve sits between the turbopump main chamber for throttling to reach higher pressures with smaller gas flows. Two Sierra SmartTrak 100 mass flow controllers (MFCs) are connected to a single gas input line into the main chamber. The MFCs are rated for ten gases, including hydrogen, helium, nitrogen, and argon, and regulate flow rates of 0.1-10 sccm. Opposite

of the gas input line is an up-to-air valve for evacuating the chamber when there is a sample exchange or required maintenance. Below these components are two pressure gauges. The first gauge is a standard full-range pressure gauge with a range of 10^{-9} Torr to atmosphere. The second is a specialty baratron gauge with a range of 7.5×10^{-6} – 8.2×10^{-2} Torr. True pressure readings from the baratron gauge provide accurate pressure signal data in the range where the full range gauge switches from Pirani to Cold Cathode mode. The switch has some inherent error associated with it, and a true pressure reading solves this issue by being a measurement technique that is gas independent. The other available ports on the main chamber are used for the LMDI, LIBS, and TDS systems.

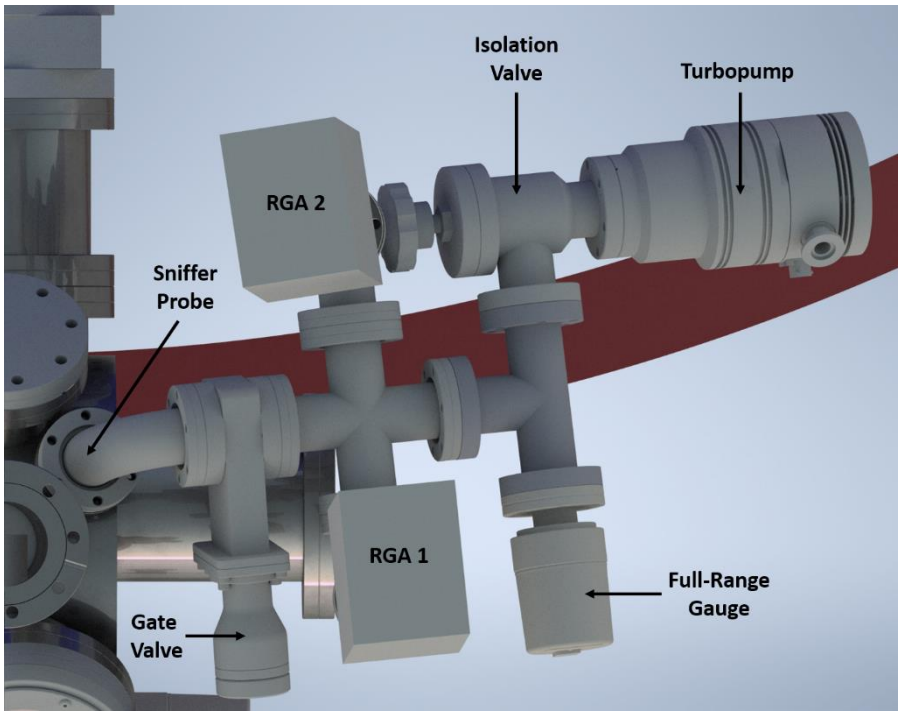

Figure 4. A CAD of the HIDRA-MAT sniffer section that houses the dual-RGA system which is used for TDS and He/D_2 differentiation.

The TDS system utilizes both the main chamber and a second section designated as the sniffer section. The sample is positioned on top of a UHV sample heater connected to the transfer arm in the main chamber. The sniffer section comprises two RGAs, a full range pressure gauge, a turbopump backed-up from a rough pump, a DN40CF gate valve, and a sniffer probe. Performing

TDS carries the concern that the sample may desorb enough particles that raise the pressure in the main chamber to a level that damages RGA filaments that can only operate as high as 1×10^{-4} Torr. The sniffer probe, labeled in figure 4, has a simplistic design to execute a specific function. It consists of a solid blank copper gasket with a 1 mm sized orifice in the center. This gasket restricts flow between the main chamber and the sniffer section. Differential pumping can be achieved because of the size of the orifice and turbomolecular pumps on both sides of the sniffer probe. The current HIDRA-MAT setup has the sniffer probe at the connection point between the main chamber and the sniffer section. This location allows for differential pumping but is planned to be moved up to the gate valve connection point on the main chamber side. The sniffer probe's new position will reduce air volume that needs to be pumped out by the main chamber turbopump through the sniffer probe's orifice when the sniffer section gate valve is closed. This change will lead to a faster pump down of the main chamber when the sniffer section gate valve is closed. Differential pumping ensures that any rise in pressure from the desorption of molecules from the sample surface will not raise the sniffer section's pressure to a pressure that damages the RGA filaments. With the sniffer section gate valve closed, a base pressure of 3×10^{-8} Torr has been recorded in the sniffer section. If throttling of the main chamber gate valve is done (partially closing the gate valve to restrict flow into the turbopump), then pressures in the main chamber can reach up to 50 mTorr before the RGAs must be turned off.

2.3 Preparation and Diagnostic Systems Overview

Sample heating is required for favorable wetting conditions of the sample [11] and TDS [12]. A HeatWave Labs Model 101491-01 UHV Heater with sample clips secures and heats the sample. The heater rotates vertically 180°, allowing it to be positioned normal to the HIDRA-MAT diagnostics. The rotation mechanism used a similar design as the system used to rotate the

fluorescent rod in HIDRA in previous experiments that measure HIDRA's magnetic fields [13]. Modifications of the design were made to adapt the rotation mechanism to the HIDRA-MAT system.

A liquid metal droplet injector was explicitly designed for HIDRA-MAT to prepare liquid metal PFCs for plasma exposure. The design goals were to create a compact, reliable, and robust design that could apply liquid metal droplets *in-vacuo* to various samples. The injector was designed for lithium use, but other liquid metals could be substituted. It was shown that the injector has the capability to form consistently sized liquid metal droplets and apply them to a substrate without the droplet detaching from the nozzle and falling to the sample. The results provide additional insight into the cooling and oxidation of lithium droplets under vacuum conditions. The end-use for the injector on HIDRA-MAT is to apply liquid metals to PFCs then expose them to HIDRA's plasma for plasma-material interactions studies.

HIDRA-MAT is equipped with LIBS and TDS diagnostic systems. LIBS is a minimally destructive surface technique that has an operation time of a few seconds. Raman spectroscopy was initially planned for a non-destructive method on HIDRA-MAT. Still, as data will show, it could not provide sufficient molecular bond information of the metals used in HIDRA-MAT. LIBS can be performed multiple times within a single shot of HIDRA, making it capable of yielding data on surface chemistry changes between exposures. After the sample is exposed, TDS is performed. TDS is a destructive surface technique that takes tens of minutes to hours, dependent on the set temperature ramp rate. Using the dual-RGA system, a method has been developed in tandem with the HIDRA-MAT TDS system to differentiate molecular deuterium and helium. These material characterization systems will produce relevant PMI data on deuterium and helium retention in PFCs along with other PFCs behavior when exposed to HIDRA's stellarator plasmas.

Chapter 3: Sample Preparation

3.1 Background

HIDRA-MAT is outfitted with unique sample preparation systems to position samples for various preparation and diagnostic systems. Linear motion and rotation of the sample were the first design criteria for HIDRA-MAT. For liquid metal application, the sample surface has to be heated to favorable wetting conditions, and TDS requires high surface temperatures, so a sample heater was integrated into the design. HIDRA's low heat flux means high energy ions will not be interacting with the surface. Still, a high sample temperature during exposure is needed for liquid metal PFC testing to keep the metals in a liquid state on the sample. Deuterium and helium retention studies could also require different sample temperatures. Preliminary experiments will look at porous tungsten with liquid lithium applied to the surface. All samples are required to be solid so they can be secured to the heater. The LMDI is used to apply liquid metals onto a solid substrate if liquid metal PFC testing is needed. Fast and precise sample positioning is one of many reasons HIDRA-MAT is an exceptional PFC characterization device.

3.2 Linear Motion and Rotation

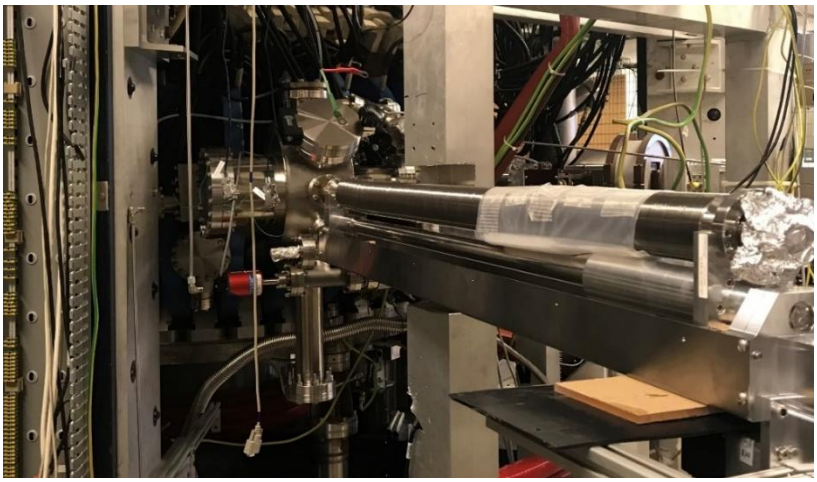

Figure 5. HIDRA-MAT's high linear shift mechanism attached to the HIDRA-MAT main chamber. The transfer arm is responsible for linear positioning of the sample for characterization and plasma exposure positions.

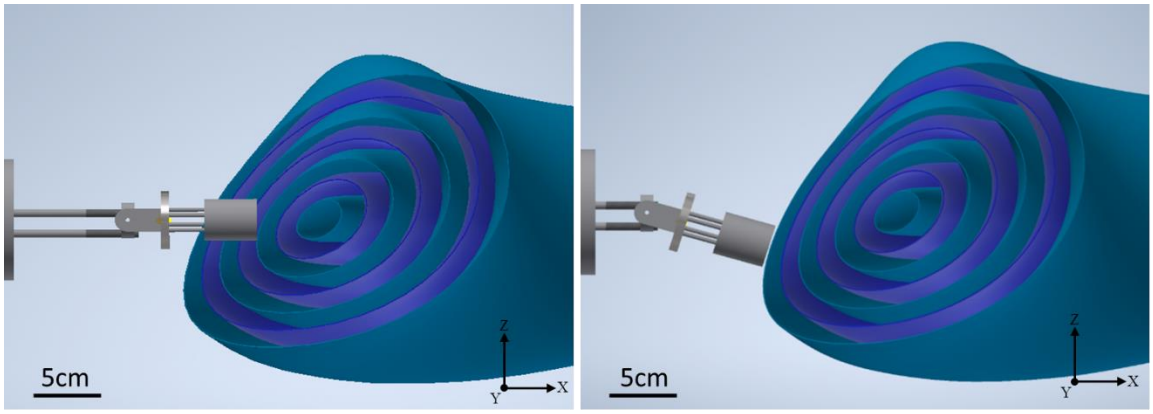

Figure 6. Full extension of (a) HIDRA-MAT's transfer arm 17.6 cm into HIDRA's vacuum vessel while a plasma is present and (b) the sample heater positioned normal to the plasma by using the sample rotation mechanism.

A sample in HIDRA-MAT is required to move linearly and be rotatable for plasma exposure and characterization. A transfer arm, seen in figure 5, provides high accuracy linear sample positioning for diagnostics and plasma exposure. A rotatable sample stage is attached to an actuated high linear shift mechanism (HLSM) with 800 mm of linear travel. Figure 6a depicts how samples can be transferred from the HIDRA-MAT main chamber through 17.6 cm of the HIDRA vacuum chamber midplane. Experiments will show how far into the HIDRA plasma the sample

can be placed before the heater elements disrupt the plasma completely. Figure 6b shows how initial experiments will expose the sample at the plasma edge, determined from magnetic field mapping and plasma shape results from previous experiments [13]. Following exposure, samples are retracted into HIDRA-MAT for surface characterization. The HLSM's micron position resolution can be taken advantage of for LIBS measurements at various sample surface locations.

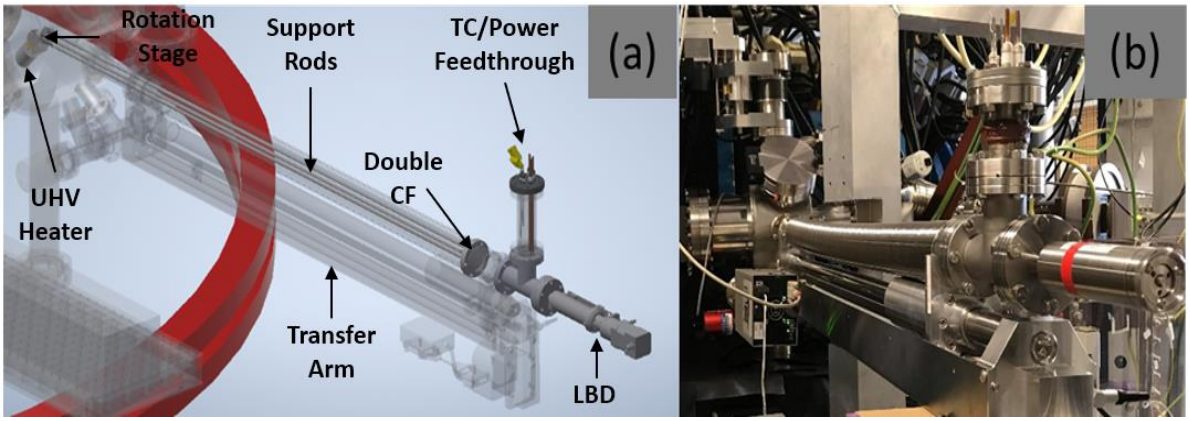

Figure 7. CAD of (a) the internal components of the transfer arm showing how the UHV heater is connected and the (b) assembled transfer arm system attached to HIDRA-MAT.

The HLSM's micron position resolution is determined by an LM10 incremental linear magnetic encoder system. This system can be taken advantage of for LIBS measurements at various sample surface locations through small linear movements of the sample to adjust the beam location on the sample. The SM23165D smart motor uses a Smart Motor Interface to set a zero position and control the HLSM by executing movement profiles. Limit switches prevent over-travel that could damage the motor. A 24 V, 8 A power supply powers the motor, and a 10-meter long cable connects the motor, power supply, and computer for operation from the HIDRA control room. The transfer arm is shown in figure 7b.

Sample heating is in HIDRA-MAT is attained using a HeatWave Labs Model 101491-01 UHV Heater. The UHV Heater can hold samples as large as 25 mm in diameter and 6 mm in height. Sample heating under vacuum conditions is expected to reach up to 1000 °C, and a built-in thermocouple connection monitors heater temperatures. The heater is mounted to a rotation

mechanism that has 180° of sample rotation. From the zero position under the lithium dropper, the sample can easily be rotated for LIBS analysis without any transfer arm motion. Rotation also gives more control of the sample's position inside HIDRA for plasma exposure ensuring the sample is normal to the plasma edge. Rotation is achieved by a connection of u-joints, a stainless-steel rod, and a linear bellows drive (LBD) with 50 mm of travel. The u-joints translate linear motion in the x-axis into rotation of the entire sample. Additionally, the sample head rotates about a horseshoe support connected to the transfer arm, so the sample head moves linearly with the transfer arm motion.

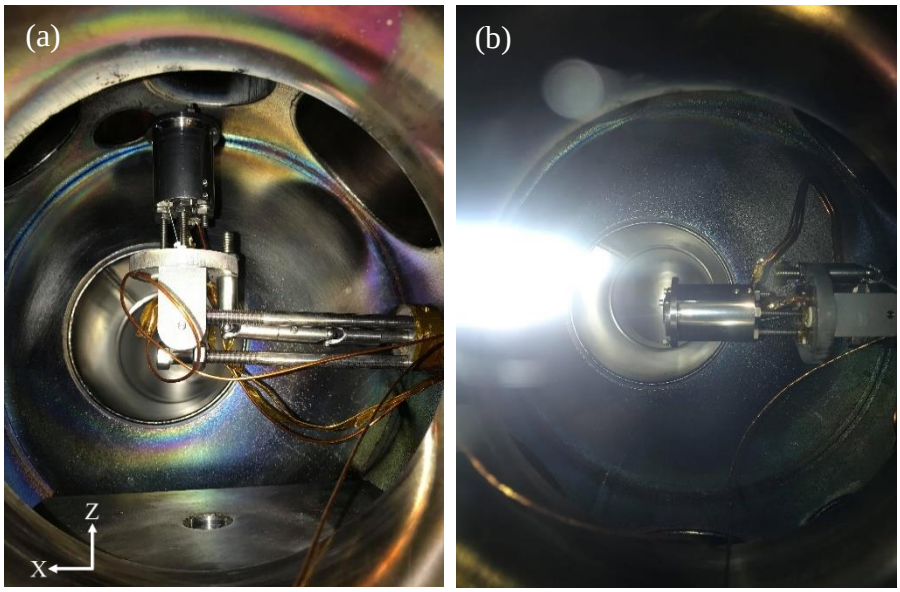

Figure 8. The UHV Sample heater in (a) a +90° vertical position used for liquid lithium application and (b) a 0° horizontal position used for plasma exposure. Rotation can continue to a -90° vertical position for 180° of rotation.

The rotation stage components are made from easy-to-machine 304 SS and are shown in figure 8 above. The UHV heater connects to the rotation stage using stainless steel threaded rods and nuts. The heater needs to be electrically isolated from the rotation stage, so power is not lost. High-temperature ceramic tubes and washers isolate the rods and nuts. Three stainless steel rods connect to the horseshoe of the rotation stage. Three support discs are equally spaced across the rods' length to add rigidity—the rods thread into a custom double-sided CF flange on the opposite

end from the rotation stage. A singular SS rod fits through the center of the flange and connects to the LBD. The other end of the middle rod is attached to the u-joints. Moving the LBD moves the u-joints and forces the stage to rotate about two pins in the horseshoe. Since the LBD movement can be controlled, the angle the sample rests at can be as well.

Wiring for the thermocouples and power is fed through the support discs and double CF flange and connected to a feedthrough located above the LBD. The thermocouples are covered in Kapton tape for isolation from the rods and discs. The atmospheric side of the feedthrough, thermocouple, and power wiring connect to a HeatWaveLabs Model 101303-23 power supply. Control and limit modules display the thermocouples' readings and can have ramp rate profiles executed from them. The modules have a $\pm 0.1°$ tolerance and work with a type-K thermocouple. The control module reads the temperature of the UHV heater's internal thermocouple, and the limit module reads the temperature from the surface of the sample. If the surface of the sample exceeds the set limit temperature, the system will shut off. The power supply can deliver up to 32 V and 47 A at full output.

Loading samples onto the heater is a quick and efficient process. The appropriate gate valves are closed, the transfer arm is retracted back to its zero position, and the main chamber is brought up to atmosphere. A DN100CF vacuum door enables easy access into the main chamber. The UHV heater is rotated into the +90° position, and samples are held in place on the top of the sample heater. There is currently no load-lock in HIDRA-MAT and no plans to install one. After sample loading, the vacuum door is closed. If liquid metals are being applied to the surface, the LMDI would have to be installed, and all of the procedures associated with doing so would have to be followed before pumping the main chamber down.

Sample transfer and replacement time rely heavily on the experiment being conducted. If the UHV heater is being used, the operator must wait until the heater cools down below 100 °C to avoid damaging it. The preparation and installation of the LMDI take approximately half a day, and when the time comes to clean and reload the LMDI, it takes another half a day. More detail on the installation process of the LMDI will be given later on. In reality, multiple samples can undergo LIBS characterization in a day, with the only obstacle being pump-down time. Assuming a plasma exposure time of ~30 minutes with LIBS characterization, the approximate time from pumping down HIDRA-MAT, running the test, and bringing HIDRA-MAT back to atmosphere to change samples is 2 hours. For a test that requires liquid metal application, plasma exposure, LIBS, and TDS, HIDRA-MAT's current threshold is one sample per day.

Chapter 4: Liquid Metal Droplet Injector

4.1 Background

Due to these properties of solid PFCs, liquid metals are being investigated as a potential alternative. In particular, liquid lithium has gained popularity due to some of its advantageous properties. Lithium is a low-Z material and has been shown to reduce plasma impurities' recycling rate increase overall plasma performance when introduced in a device [8, 14]. Furthermore, liquid metal walls are self-healing, have the potential ability to self-pump through concepts like TEMHD driven flow [7]. Ultimately liquid metals can be incorporated into a flowing loop system that can be used, in the case of lithium, for extraction of DT fuel and other impurities. These liquid metal properties serve as motivation to focus research on liquid metal PFCs.

There are various ways to introduce lithium into a fusion system. Some setups use lithium evaporation for conditioning the walls to coat the inside of the machine [15], while others inject lithium granules to target the plasma itself [16]. Certain injection systems can also introduce a powder that interacts with a plasma column and turns into an aerosol inside the scrape-off layer [17]. These systems help increase plasma performance and provide further evidence supporting the use of lithium in fusion devices.

PMI is a crucial component of the fusion energy challenge. There needs to be a greater emphasis on PMI, including a more extensive study of the plasma-liquid lithium interactions. Wetting experiments of liquid lithium applied to the underlying substrate have been conducted using droplet injectors to investigate liquid lithium properties. These experiments provide useful data on lithium behavior but lack supporting *in-vacuo* diagnostics to develop a complete understanding of the metal-substrate interfaces at play [11, 18]. The following paper will describe a new liquid metal droplet injection system in detail and discuss how it will be used in conjunction

with a new diagnostic system to provide a deeper understanding of liquid metal-substrate and plasma-liquid metal-substrate interfaces.

4.2 Design Overview

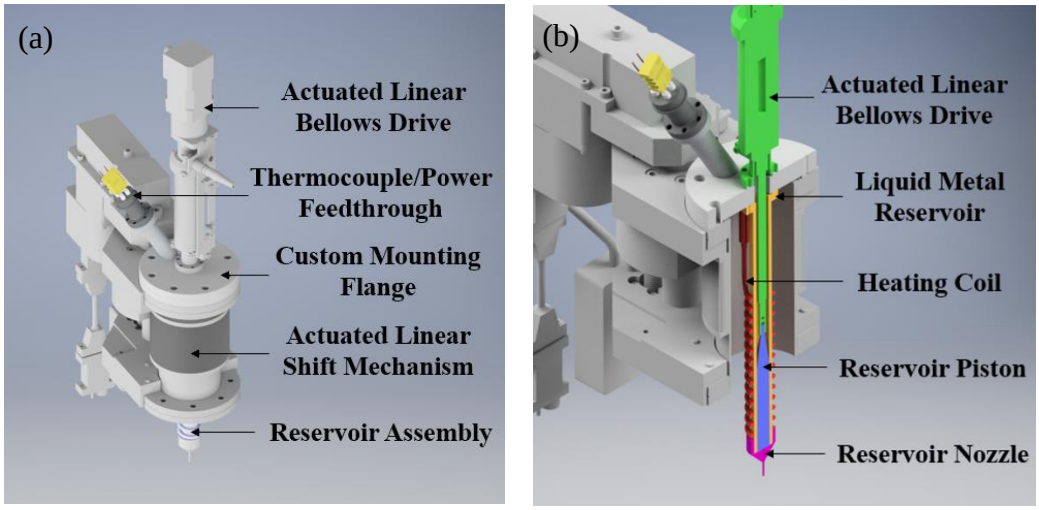

Figure 9. CAD of HIDRA-MAT's (a) LMDI for applying liquid metals to samples in HIDRA-MAT and (b) cross section view of the LMDI's reservoir assembly.

The injector design drew inspiration from UIUC and UCSD injectors that performed similar tasks [11, 18]. Though similar, HIDRA-MAT's liquid metal droplet injector was explicitly developed for use on the HIDRA-MAT chamber and required compatibility with other diagnostics and remote operation. In HIDRA-MAT, the samples will be held in place on a UHV heater at a fixed height during the droplet application. This setup demands droplet placement accuracy to avoid applying liquid metal onto heater electronics and possibly destroying them from corrosive interaction. Samples can be up to 25 mm in diameter and 6 mm in height, so the injector design requires that there is height tolerance incorporated as well as controllable droplet sizes. Compactness and robustness result in less maintenance, and when needed, parts are cost-efficient to repair or replace.

The design shown in figure 9 highlights how the injector components come together in the final assembly. Assembly involves first attaching the reservoir piston to the LBD and the liquid

metal reservoir to the custom mounting flange's vacuum side. The LBD and reservoir piston are then connected to the mounting flange's atmospheric side such that the reservoir piston is inside the reservoir. The heating coil slides over the reservoir tightly, and the heating coil leads are connected to the thermocouple/power feedthrough. Solid metal is loaded through the end of the liquid metal reservoir. An argon environment is used when loading lithium to mitigate oxidation. After loading the metal, the reservoir nozzle is screwed on, and the injector is installed onto the actuated linear shift mechanism (LSM), which remains on the HIDRA-MAT chamber. Supporting electronics and power supplies for the actuation and data collection are then connected, and the injector is ready to start the injection process.

The vacuum chamber is pumped down to pressures within a magnitude of 1×10^{-3} Pa or lower. In the case of lithium, the heater is brought to a temperature of ~220 °C (T_{melt}, Li = 180.5 °C) indicated from the thermocouple inside the coil heater. This process takes over an hour with the setup to ensure the whole reservoir assembly is adequately heated. To create a droplet, the actuated LBD moves the reservoir piston and pushes the liquid metal out of the reservoir nozzle. Distance from the nozzle to the substrate can also be adjusted by moving the LSM in the z-direction.

4.3 LMDI Component Details

Actuated Movement

Versatility and safety come from the injector's actuation. All component movement can be controlled from a distance by running set programs from a control computer. The LSM is an LSM64-50-SADC with 50 mm of travel enabling droplet application to samples of various heights. It also makes it possible to apply a droplet to the sample without detaching from the nozzle and falling to the sample. Physically dropping the metal onto the substrate could cause an unwanted

droplet break up onto heater components. It should be noted the LSM stays installed on the vacuum chamber by a DN63CF connection, and all the other components are attached via the DN63CF mounting flange after the metal has been loaded in the reservoir. The other actuated element is the LBD, which is an LBD16-50-IS with 50 mm of travel and a DN35CF connection. At the full stroke length, the piston's position is at the end of the reservoir, reducing metal waste.

Heating Coil System

Heating is done by a custom TEMPCO Mightyband Coil Heater with a built-in type K thermocouple surrounded by MgO insulation. The heater can reach temperatures above 1000 °C, though, for this application, a maximum of 300 °C is required. The power and thermocouple leads are covered by a 304SS sheath, except for the connection points to the feedthrough. Connections are covered in Kapton tape during installation for more robust connections and electrical isolation. The coil fits tightly around the liquid metal reservoir but has enough bend to be taken off. The nozzle prevents the coil from sliding off the reservoir. The heater's power and thermocouple lead connect via a feedthrough connected to the power supply and thermocouple reader. The thermocouple is located at the end of the coil and rests on the top of the nozzle. The thermocouple placement gives a general idea of the liquid metal temperature in the reservoir but is not the actual temperature. It has been seen that the nozzle tip takes much longer to heat up than the reservoir due to the low thermal conductivity of stainless steel. To overcome this problem, a metal wire with higher thermal conductivity (Al, Cu) can be wrapped around the reservoir and nozzle to promote heat transfer. The molten metal in the reservoir and nozzle also help with heat transfer to the nozzle.

Reservoir Assembly and Injection of Droplets

The reservoir assembly comprises the liquid metal reservoir, reservoir piston, reservoir nozzle, and heating coil. These components attach to the custom mounting flange and the actuated LBD for liquid metal droplet injection. Keeping lithium use in mind, the design accommodated all reservoir assembly components with 304SS for stronger corrosion resistance. Each component is separate from one another, so cleaning is made easier. If a component needs to be repaired or replaced, the whole injector does not have to be replaced, saving cost over time.

The liquid metal reservoir is a bored-out 304SS rod threaded at one end, and at the other end, a DN16CF connection is welded on. The threads outside the reservoir help slow lithium from creeping up the nozzle walls and spilling into the vacuum chamber. If the threading were on the inside of the reservoir, gravity would aid lithium creep, and lithium could cover the outside of the nozzle. The nozzle's design came from previous designs of other injectors at UIUC [11]. It is expected that different variations of nozzles will be fabricated and used with the injector. Specific dimensions were chosen based on sample position in HIDRA-MAT.

Connecting the LBD and the liquid metal reservoir is the custom mounting flange. The flange is a DN63CF to DN16CF zero-length reducer that has been modified for this application. Modifications include another DN16CF connection on the flange's vacuum side with tapped holes so the liquid metal reservoir can be attached. A hole was drilled through the flange, and then a half nipple with a DN16CF connection on one end for the feedthrough connection was welded onto the flange. On the atmospheric side of the flange, the LBD is connected to keep the vacuum, but on the vacuum side, the connection does not contribute to keeping the vacuum, so an old gasket is used. The connection point provides an escape for any pressure that may build up in the reservoir when heating the metal.

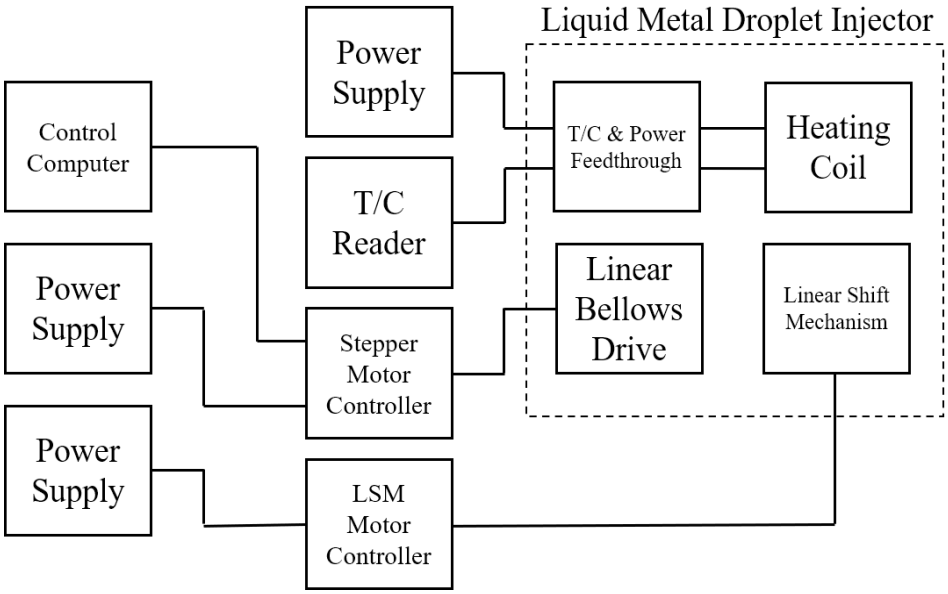

Figure 10. Schematic of wiring connections for the liquid metal droplet injector.

Droplets are produced by driving a piston with the LBD through the reservoir to push the molten lithium out of the nozzle. The piston is tapered and threaded at one end so it can be screwed into the LBD. The piston's diameter was manufactured to the reservoir's inner diameter such that it was snug but still able to move through it. The LBD is connected to a computer through a Nanotec Electronic C5-01 open-loop stepper motor controller to control an executed program's actuation. Actuation paired with the high surface tension of lithium allows for small steps to be made by the piston to start the droplet's formation while still attached to the nozzle. Subsequent piston steps grow the droplet to the desired size, and then the LSM is used to lower the droplet to the sample. Figure 10 above shows all the electrical connections for the injector.

4.4 Experimental Setup and Results in Temporary Chamber

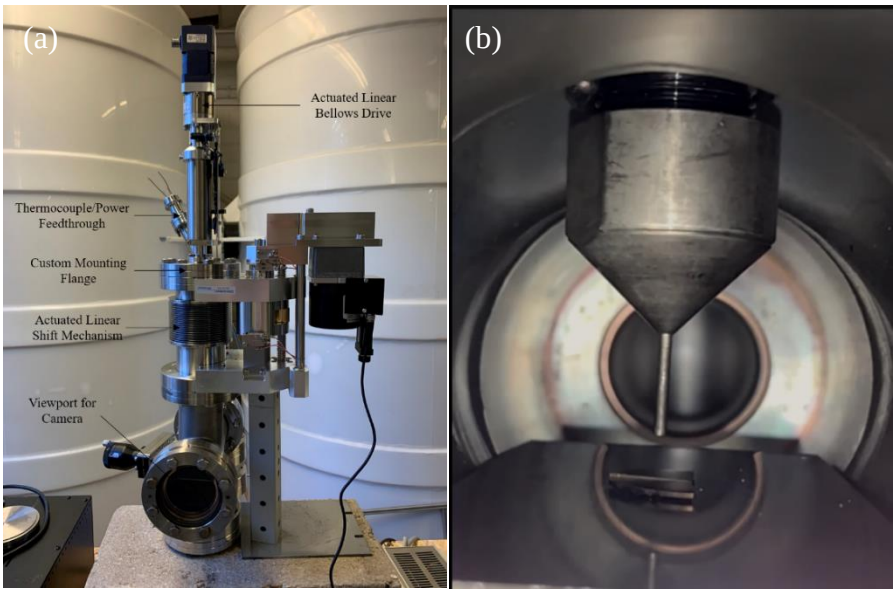

Figure 11. Experimental setup (a) of the liquid metal droplet injector (b) camera view looking at nozzle position and a tungsten sample.

The injector setup shown in figure 11a was used to test droplet injection. A test setup was used instead of HIDRA-MAT because we wanted to limit the lithium amount introduced to HIDRA-MAT. This temporary setup provided all the necessary features to confirm that the injector will work when installed on HIDRA-MAT. Unannotated in figure 11a is the gate valve, turbomolecular pump, rough pump, and supporting electronics. The supporting electronics for supplying power and reading/sending data were connected after installing the injector onto the vacuum chamber. An external thermocouple monitored the temperature of the bellows during the heating of the coil.

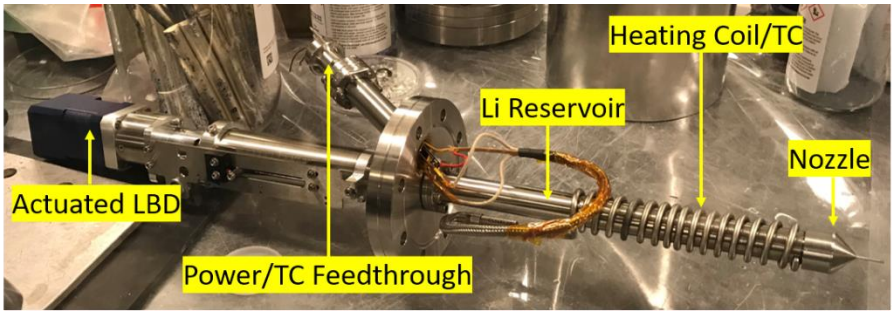

Figure 12. The liquid metal droplet injector in the lithium loading glovebox which provides an argon environment to mitigate oxidation of the lithium.

Before the lithium dropper could be installed onto the vacuum chamber, it needed to be loaded with lithium. Loading was done in an argon environment and then transferred to the vacuum chamber. Figure 12 is the liquid metal droplet injector in the glovebox after the lithium has been loaded. The opening at the nozzle tip is covered during the transfer process to limit the oxidation of lithium. Purity is not a concern for these tests since the oxidation that would occur during installation will not influence droplet formation. Furthermore, lithium use in commercial devices will have to deal with oxidation concerns, so there is validity to allowing oxidation to mimic those conditions better. If purity did become a concern, the design would have to change to include a vacuum suitcase for transferring.

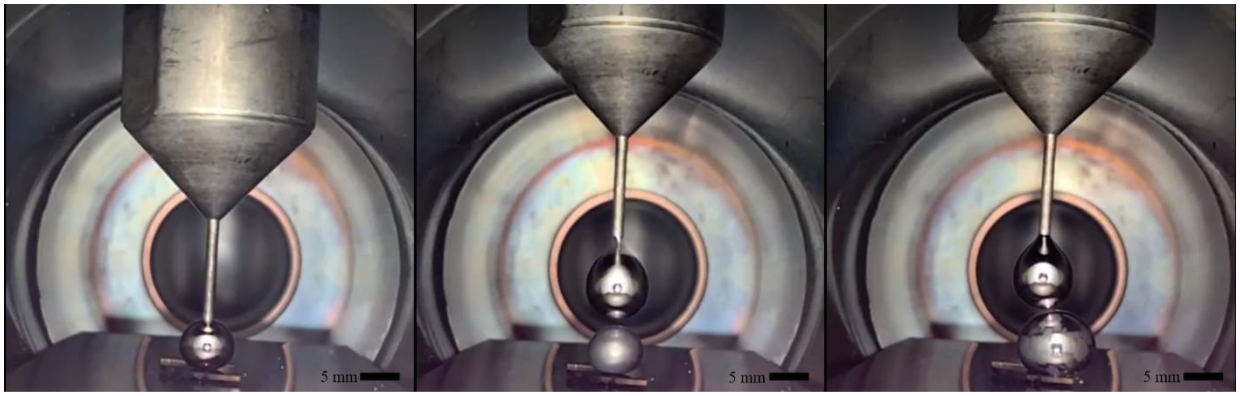

Figure 13. Three droplets were produced during the experiment and their size was measured through ImageJ software.

Droplet diameter had a range of less than 1 mm for the three droplets created portrayed in figure 13. For future planned tests, this is an acceptable range. The experimental procedure can explain the difference in droplet diameter. Droplet 1 was formed, and surface tension kept it attached to the nozzle. The droplet was then lowered to the surface of the sample using the LSM. Once in contact with the substrate, the nozzle was retracted, and the droplet was left on the surface. If the sample were heated, it would be expected that the droplet would more easily transfer to the sample through wetting.

Droplet 2 was formed with the nozzle retracted and sitting above the first droplet. Droplet 2 grew until it coalesced with the first droplet. Coalescing of the droplets demonstrated that even with the droplet's impurity growth, it had not cooled off or hardened between droplets. The same effect was present for the application of the third droplet. Droplet 3 had a smaller diameter than droplet 2. With the same actuation step program, it would be expected that each droplet would be the same. However, the combination of the first two droplets reduced the distance between the nozzle and the sample. The reduced space caused the droplet to interact sooner, so the measured diameter was smaller. If there were room for the full droplets to form, less dissimilarity in diameters would be anticipated.

Figure 14. Five points in time were chosen since the first droplet was applied (a) Right at the time of application of the droplet to the sample (b) Letting time pass to observe oxidation (c) Addition of a new droplet (d) Addition of another droplet (e) Letting time pass to observe oxidation.

Figure 14 highlights the effects of lithium oxidation in vacuum conditions. The application of the droplet to the substrate is the first stage seen in figure 14a. At the time of application, the droplet is physically hot and has a reflective shell. As the droplet sits on the substrate, it will start to cool and undergo oxidation. After one minute, lithium oxidation could be observed by the change in the droplet's shell from reflective to dull in figure 14b. Lower pressure would slow this oxidation effect. The addition of a second droplet in figure 14c, four minutes after the first droplet, reveals that the first droplet had not become solid. There is a clear distinction in the shell of the two-droplet mass between the shell parts that belonged to the first droplet and those of the second molten droplet. Figure 14d is directly after the addition of the third droplet. The third droplet was added one minute after the second. The shell from the first droplet can still be distinguished, and

the cooled and oxidized sections are in different positions of the lithium mass. It was observed that these cooled and oxidized shell parts rotated on the shell of the lithium mass when a new droplet was added. Furthermore, figure 14e was taken two minutes after the third droplet giving it time to cool and oxidize in the vacuum environment. It can be seen that the coalesced droplet is starting to cool and oxidize, but even so, parts of the first droplet's shell can be observed in this last documented stage. Once the droplet was brought to atmosphere, the outer shell took on a more uniform look.

4.5 Experimental Setup and Results in HIDRA-MAT

Once proof of concept was demonstrated, the LMDI was installed onto HIDRA-MAT for a wetting experiment. The experiment's objective was to show the LMDI's lithium droplet capabilities to a heated substrate in HIDRA-MAT. A 1" diameter lithiated porous tungsten sample was secured to the UHV heater using the sample clips. The clips were placed in such a way to minimize the chance of lithium interacting with them. The porous sample had a lithium film thickness of approximately 50-100 nm. The sample was lithiated a year prior to the experiment, so the surface had been fully passivated. A thermocouple was placed on top of the UHV molybdenum heater to ensure the sample was heated and confirm the other thermocouple's readings on the heater's underside. During the experiment, the thermocouple at the top of the UHV heater shifted and became lodged between the heater's heat shield and side. Securing the thermocouple under the sample will be done in the future.

The preparation of the lithium was done in a glove box with an Argon atmosphere. A lithium rod was cut into an inch long piece and placed in the lithium reservoir. Then the nozzle was screwed onto the reservoir. The LMDI was then transferred from the glove box to HIDRA-MAT to be installed onto the LSM. Purity was not a concern, so there was no need to pump argon

into the HIDRA-MAT chamber during installation. After installation, the chamber was pumped down.

HIDRA-MAT was pumped down to a base pressure of 3.55×10^{-7} Torr after a 48-hour bakeout of the UHV heater at 400 °C. The UHV heater was brought up to 300 °C and held at that temperature for 4 hours to let the sample outgas. In future experiments, this outgas step would not be necessary. After the sample temperature reached 300 °C, the lithium reservoir was brought up to a temperature of 235 °C over 1.5 hours. This preparation can be done in a shorter timeframe by raising the UHV heater and heating coil temperatures, but the precaution was taken on this first experiment to avoid significant outgassing that could damage any equipment. After the UHV heater and heating, the coil had been heated to their required temperatures; the HIDRA-MAT chamber was at a pressure of 2.02×10^{-5} Torr.

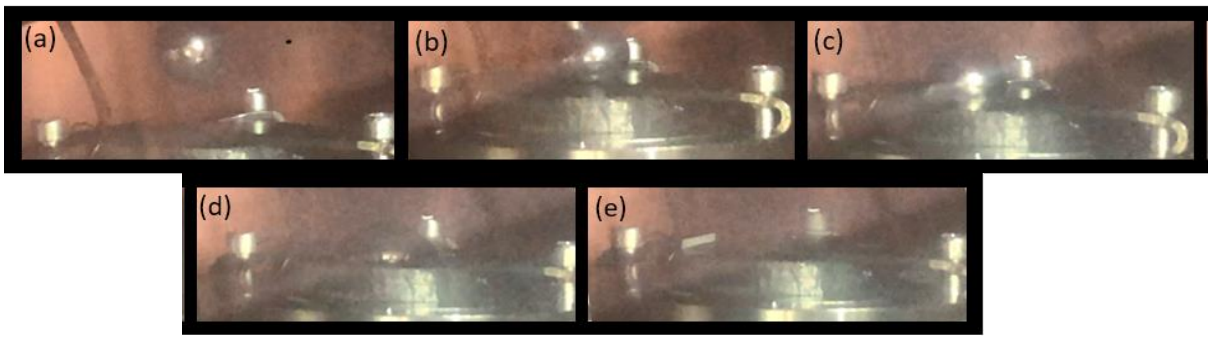

Figure 15. Stages of the lithium droplet to the heated porous tungsten substrate. The (a) first stage is of the lithium droplet above the substrate attached the LMDI nozzle before (b) the droplet contacts the surface but is still connected to the nozzle. The nozzle is then retracted upward and (c) the droplet detaches from the nozzle and rests on the sample surface. Shortly after detachment the (d) droplet starts to wet the substrate before (e) completely sinking into the porous structure.

With a steady pressure in the HIDRA-MAT main chamber, the RGA was turned on to measure any effects the LMDI application might have. A droplet was formed on the tip of the nozzle and then slowly lowered to the heated surface. The droplet contacted the sample surface, and the nozzle was then raised, which had the effect of the droplet detaching from the nozzle. The droplet then wet the surface and sunk into the pores of the sample. Figure 15 shows the stages of

application of the droplet to the sample. The sample was then rotated to a horizontal position to demonstrate lithium's surface tension on the sample. The rotation was successful aside from a heater lead detaching during the process (The attachment was not fully secured and has since been fixed). No lithium was observed to depart from the sample. Further testing with non-porous samples would demonstrate the surface tension properties more clearly.

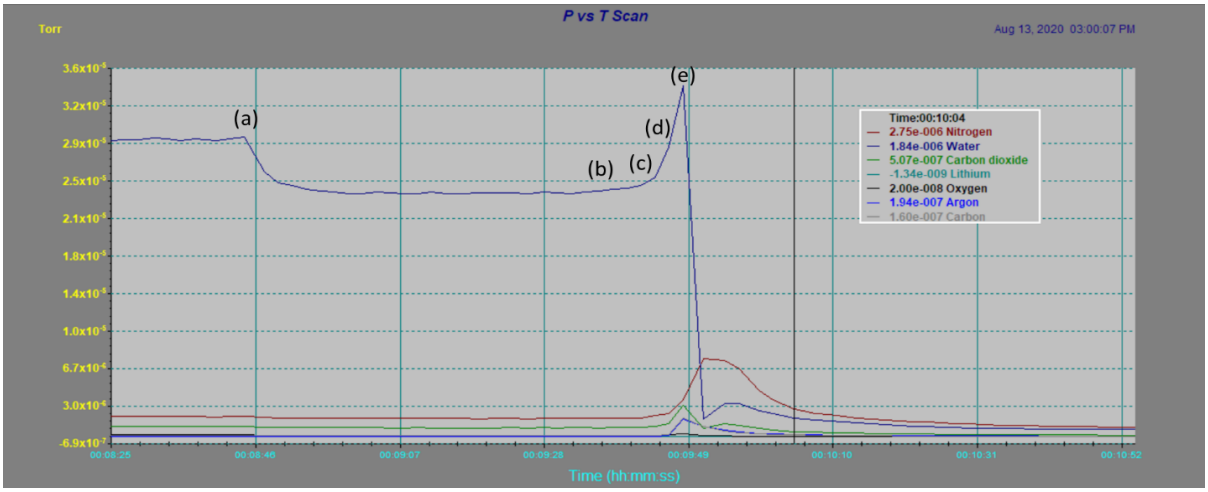

Figure 16. RGA partial pressure tracking for various masses (N_2, H_2O, CO_2, Li, O_2, Ar, and C). The water partial pressure line is annotated corresponding with figure 15 to show how the water signal responded with the application of the lithium droplet.

The RGA tracked partial pressures of N_2, H_2O, CO_2, Li, O_2, Ar, and C during the droplet application. During the experiment, the RGA data scan was not monitored. Conclusions on the RGA data were made from a video of the application. Figure 16 shows the RGA partial pressure signals during the droplet application. The line of interest is the water signal because lithium and water are highly reactive. Oxidation occurred once the lithium droplet started to form on the nozzle relating to the initial drop of the water signal at part (a) of figure 16. With the chamber's pressure at 2.02×10^{-5} Torr, monolayers formed at a rate of approximately ten monolayers/sec. The droplet resided attached to the nozzle for 50 seconds before it contacted the substrate, where a rise in the water signal is observed at part (b). Over the next 13 seconds, the water signal rose to a peak at

part (e) of figure 16, then sharply dropped an order of magnitude in 3 seconds. Part (e) signaled the moment the droplet had sunk entirely into the porous tungsten.

The cause for these signal changes is directly attributed to the interaction between droplet and substrate. It is observed that when the droplet was formed on the nozzle and not in contact with the substrate, the only change in signal was water. Once the droplet was applied and started to sink into the substrate, signal changes in N_2, H_2O, CO_2, Li, O_2, and Ar were present. Data collected does not provide conclusive evidence on the physical mechanisms at play; however, a hypothesis can still be made on the lithium-substrate interaction's general phenomena. The images in figure 15 paired with the RGA data in figure 16 may describe the interactions happening in the substrate's pores. The sample was previously lithiated with less than 100 nm of lithium before the droplet was applied. The sample surface temperature measurement was subject to potential inaccuracies. It is viable the surface was less than the 235 °C lithium or the droplet had sufficiently cooled as it sat on the nozzle. The rise in water signal could indicate a cooling of the droplet once the droplet touches the surface. Cooled lithium is less reactive with the water in the chamber, and the pressure starts to rise. A few seconds after the droplet touches, bonds of surface oxides begin to break down from the hot lithium droplet resting on the substrate's surface while it is still attached to the nozzle. The droplet then detaches from the nozzle and wets the substrate surface. The droplet spread introduces more hot lithium to the chamber that was previously at the core of the droplet shielded by the formation of monolayers and potential cooling. A hot core of lithium with an oxidized shell was previously demonstrated by previous experimental results shown in figure 13. The newly exposed lithium is highly reactive with the water in the sample and the chamber and significantly drops the water signal. The signals then rise slightly before slowly falling to levels at which they are steady except for the water signal, which falls at a slower rate. The peak and fall of

the N_2 signal are delayed compared to the other partial pressures and most likely have something to do with the breaking of oxide bonds on the surface and in the tungsten substrate's pores. As noted, the water signal falls for 70 seconds then slowly begins to rise. This gradual decline in the signal may be attributed to the droplet moving through the sample pores and reaching the heater. The lithium would then stay at a temperature where it could react with the water in the chamber for a more extended period before eventually cooling or becoming saturated.

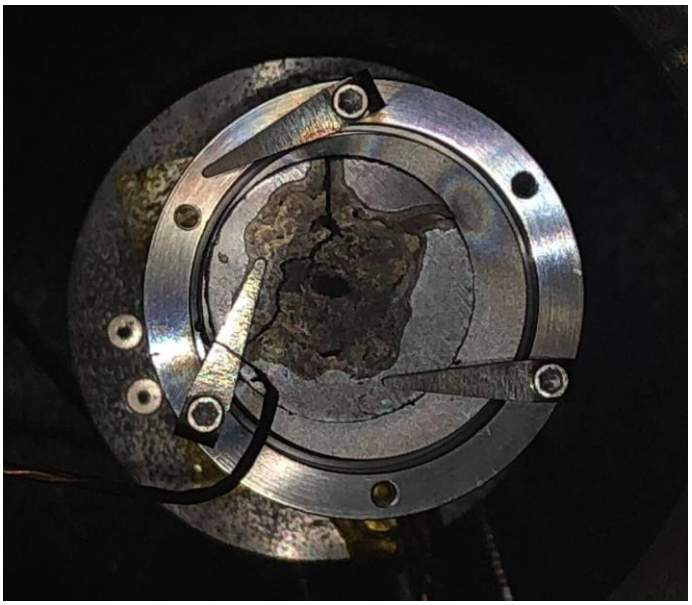

Figure 17. Top-view of the lithiated porous W sample in atmosphere after lithium droplet application. The droplet spread as it traveled throughout the sample's pores can be seen. The droplet broke the sample into three pieces and the break is at the dark lines.

Figure 17 displays the sample surface post-application after the sample had been exposed to atmospheric conditions. During the sample's removal, it was noticed that the sample had split into three separate pieces. Thermal shock during droplet application, lithium corrosion of the pores, or other factors could have caused this break. The surface's wetting is shown in figure 15, providing further insight that the substrate's capillary porous structure could direct flow in different directions. The sample was rotated from a +90° orientation to a horizontal 0° orientation to observe the lithium's surface tension properties. No lithium fell from the sample, but gravity is

the most probable reason for the lithium concentration to be greater at the top of the sample, as depicted in figure 17, compared to the bottom.

Overall, the LMDI has demonstrated to be in working order on both a temporary setup and the HIDRA-MAT chamber. Lithium droplet size can be controlled by adjusting piston step length, and the surface tension of lithium keeps the droplet attached to the reservoir nozzle. The application of the lithium to the substrate is straight forward through control of the LSM. The droplet stays together and does not break up during the application process allowing for more consistency between tests. Finally, the UHV heater makes it possible to wet samples before plasma exposure enabling testing to be done on PFCs incorporated with liquid metals in HIDRA.

Chapter 5: Thermal Desorption Spectroscopy

5.1 Background

TDS is a commonly used technique within the scientific community due to its straightforward setup and extensive literature on the technique. TDS works by ramping up a substrate's temperature, thus providing energy to break surface bonds, to desorb atoms and molecules from its surface. In HIDRA-MAT's setup, RGAs in the sniffer section provide data on what atoms and molecules are being desorbed by identifying each atom and molecule's mass to charge ratio. Relating the temperature data to the mass pressure data from the RGA produces a plot that can be used to quantify the amount of each molecule that is desorbed from the sample. In conjunction with helium/deuterium differentiation and LIBS, TDS will compare data to provide accurate quantification of the amount of deuterium desorption from PFCs.

Experimental results from Taylor et al. [10] show that deuterium desorbs from tungsten around 600K. HIDRA-MAT's UHV heater can reach much higher sample temperatures than is required to desorb this deuterium. In general, TDS samples will be tested before and after exposure to establish a control for each experiment. Another essential factor to consider in deuterium retention studies is the desorption of deuterium between characterization. Desorption rates of deuterium in tungsten are heavily dependent on material structure and thermal conditions [19]. Desorption rates must be accounted for so accurate calculations can be made attempting to quantify the deuterium retention in any sample. Experiments from Jiang et al. [20] on deuterium outgassing have characterized the deuterium content in a tungsten sample after plasma exposure has been completed and shown that deuterium content does fall off significantly over tens of minutes. As experimental campaigns on HIDRA-MAT are pursued, these deuterium losses will be applied in TDS and LIBS data analysis.

5.2 Heater Design and Experimental Results

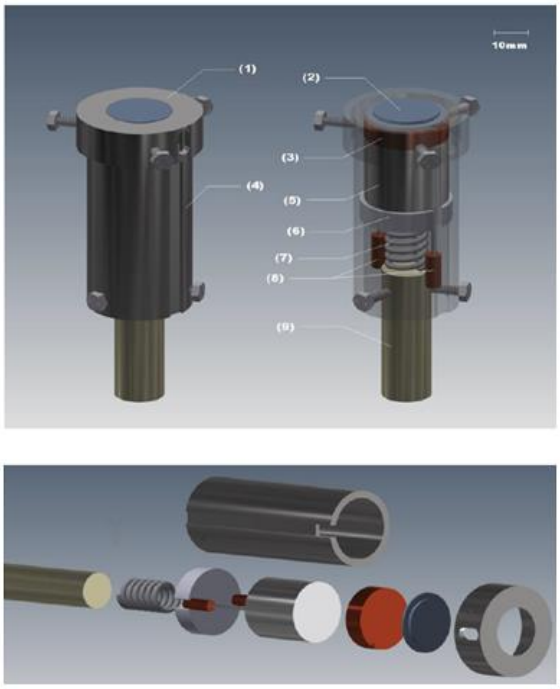

Figure 18. CAD of the original sample heater that was used for TDS in HIDRA-MAT.

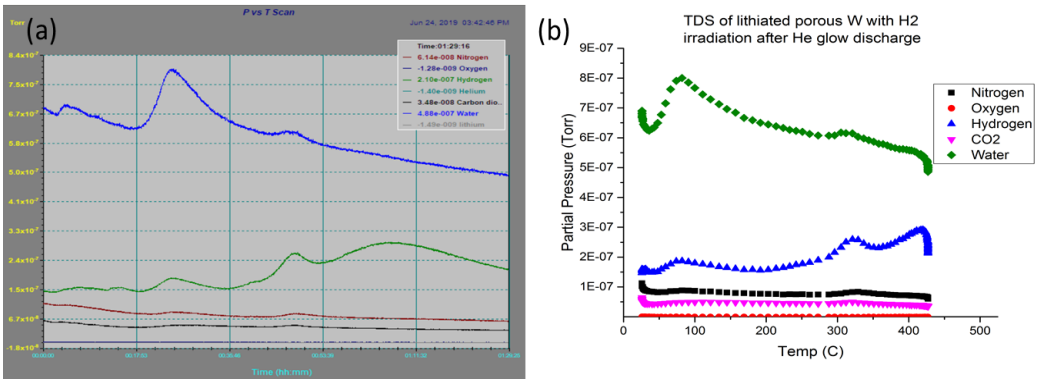

Figure 19. TDS data of a D_2 irradiated porous W sample showing (a) RGA data on mass partial pressure vs. time and (b) the mass partial pressure vs. temperature as a function of time. The data shows the expected peak of deuterium desorbing from the sample at ~337°C *[12]*. Credit to Zacharia Koyn for help on data analysis.

Two UHV heater versions were explored in HIDRA-MAT for TDS. The first heater was a HeatWaveLabs Inc. Standard Series Cartridge Heater capable of reaching temperatures of 1200 °C in UHV. This model included two power leads, one input and output, and required an outer casing to be manufactured to support it inside of HIDRA-MAT. This casing support's design and

fabrication were done outside this thesis work but were used in TDS's initial testing in HIDRA-MAT. This heater's design can be found in figure 18, and TDS data collected from a deuterium irradiated tungsten sample after a He glow discharge is shown in figure 19. The peaks seen in mass four desorption align with deuterium desorption values in literature.

The original heater design included a stainless steel outer shell that housed the cartridge heater, copper disc, and sample. A cap was placed over the end of the housing to hold the sample in place and was secured by a set screw. Modifications to the original design of HIDRA-MAT made it evident that the sample securing mechanism was insufficient due to the difficulty of positioning the sample for experiments, specifically on the need for samples to be manufactured into a specific shape be used for experiments. The main issue that arose was the heater's inability to reach temperatures past 500 °C. The stainless steel shell around the heater acted as a heat sink, and the sample could not reach the desired temperatures. This issue forced the heater to be replaced by a design that could reach the necessary temperatures and function in the capacity HIDRA-MAT intended to use it. It solves the major issues found in the original design by including a heat shield, so heating is directed towards the sample and securing the sample using sample clips, allowing various samples to be used and limiting support structures from interacting with the plasma during exposure.

A crucial part of introducing a functional TDS system in HIDRA is controlling the heater and sample temperature ramp rate. To accomplish fine control of heater temperature, a HeatWaveLabs Model 101303-23 power supply was refurbished and added to the TDS system. The power supply can control heater temperature to a tolerance of $\pm 0.1°$ and has the option to set a programmed temperature profile. An internal thermocouple is placed on the heater's backside, and an external thermocouple is placed on the sample or top of the heater. Heat losses between heater and sample

are expected, highlighting the need for external thermocouple's placement to indicate the sample temperature and not the heater.

Being a destructive characterization technique, TDS will be used after plasma exposure and to verify LIBS measurements. The sample temperature will be brought to 1100 K, and heating will be linear as a function of time. Running the RGA in pressure vs. time mode allows for multiple species to be looked at simultaneously. The interaction between lithium and hydrogen will also be investigated when TDS is done with liquid metal PFC samples that were exposed to hydrogen plasmas. LiH comes in two forms where hydrogen dissolves into the liquid lithium (α phase) or a precipitate forms (β phase), and these phases' desorption are dependent on temperature [21]. The α phase is unbound and desorbs at temperatures around 400 °C while the bound β phase desorbs at higher temperatures around 600 °C as shown by Christenson et al. [22]. Comparing TDS peaks from experiments conducted in HIDRA-MAT to those already done with LiH will provide a better understanding of the interaction between the lithium, hydrogen, and PFC material. Helium and deuterium differentiation during TDS is also possible through the dual RGA system described in detail in the next section.

Chapter 6: HIDRA-MAT Dual RGA System and He/D_2 Differentiation

6.1 He/D_2 Differentiation

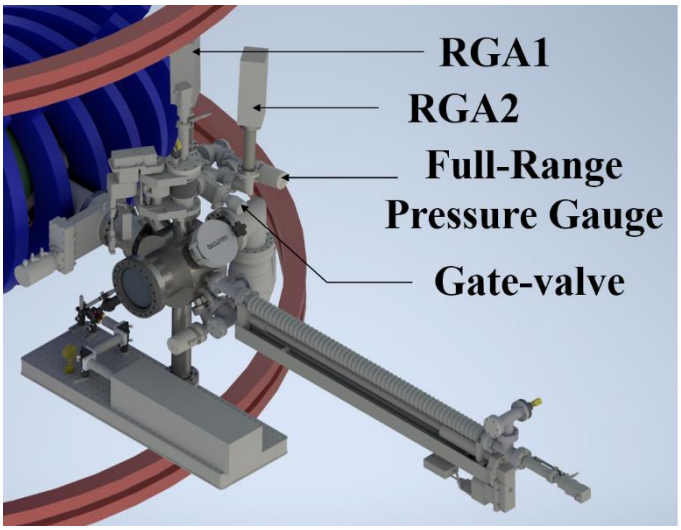

Figure 20. CAD representation of the final HIDRA-MAT assembly with sniffer section components labeled. The sniffer probes location is between the gate valve and main chamber.

D_2 and He PMI are of deep concern when considering fusion applications. These products and reactants will collide with the walls at high energies within a fusion reactor and potentially implant themselves in the PFCs surface. It is crucial to understand the retention behavior of PFCs when it comes to interactions between PFCs, D_2, and He. He implantation in tungsten PFCs has shown to lead to bubble formation under the surface. Over prolonged exposure, ion implantation leads to tungsten fuzz formation, which can have detrimental effects on plasma performance [23]. When D_2 becomes implanted in the device's walls, it causes fuel to be lost to the walls with no way of reintroducing D_2 into the system. The retention behavior of PFCs becomes more pertinent when tritium is considered because PFCs with implanted radioactive isotopes pose a greater challenge to maintain and replace. Developing PFC's that address these problems and limit retention of particles from the plasma will lead fusion closer to reality.

D_2 and He have remarkably similar masses, so the SRS100 RGA's resolution cannot distinguish them from one another. This similarity in mass makes it difficult to characterize materials without having to buy expensive diagnostics. However, the HIDRA-MAT dual-RGA system enables the masses to be distinguished at a fraction of the cost using a technique similar to RGA mass differentiation used on EAST [24]. The dual RGA setup's geometric configuration necessitated each RGA was the same distance from the particle sources and sinks inside HIDRA-MAT, as shown in figure 20. Each RGA is the same distance from the sniffer probe and the turbopump. The particles have to follow the same distance and path to reach the RGA, ensuring that if set at the same electron energy, they should read similar partial pressures. More accuracy could be achieved through peak tuning each RGA.

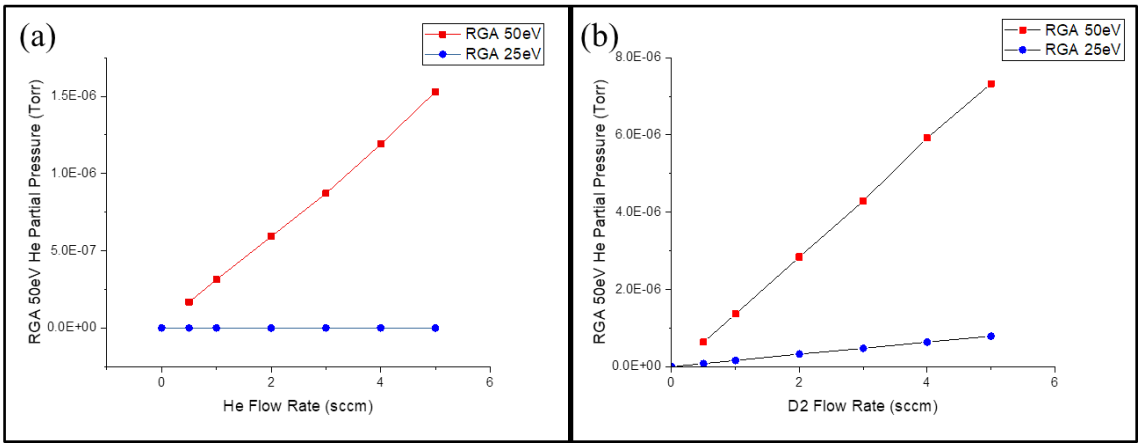

Figure 21. Raw RGA data for (a) mass 4 partial pressure vs. He flow rate and (b) mass 4 partial pressure vs. D_2 flow rate. Data showing the RGA set at 25 eV shows no mass 4 signal when He is introduced into the HIDRA-MAT chamber. The same 25 eV RGA shows a mass 4 signal when D_2 gas is introduced into the HIDRA-MAT chamber.

The process of differentiating D_2 He gas begins with choosing the ionization energies of the RGAs. The ionization potentials of D_2 and He are 15.46 eV and 24.58 eV, respectively. One RGA is set to 50 eV having the effect of ionizing both D_2 and He. 50 eV was purposefully chosen as the electron on the RGA to avoid doubly ionizing He at its second ionization energy of 54.41 eV while maximizing the RGA signal. A second RGA set to an electron energy of 25 eV, the lowest possible setting on the RGA100, results in a negligible signal when trying to read an RGA He partial

pressure but produces a significant RGA partial pressure signal when reading D_2, as seen in figure 21. This differentiation can be used to determine the percentage of D_2 that makes up the 50 eV signal to ionize both D_2 and He.

6.2 Differentiation of Gas Mixtures

To demonstrate He/D_2 differentiation further, the dual-RGA system was used to identify He/D_2 gas mixtures. The goal of the experiment was to determine the mixture composition using just the signals obtained from the RGA. The first step involves calibrating the RGAs for pure gas flows. To minimize error in the measurements, it was most straightforward to collect data to produce calibration curves to relate true gas pressure to the RGA signal. By doing so, it allows for the mixture concentration to be identified by converting RGA signals into physical gas pressure values and then calculating mixture composition, which will be explained in this section.

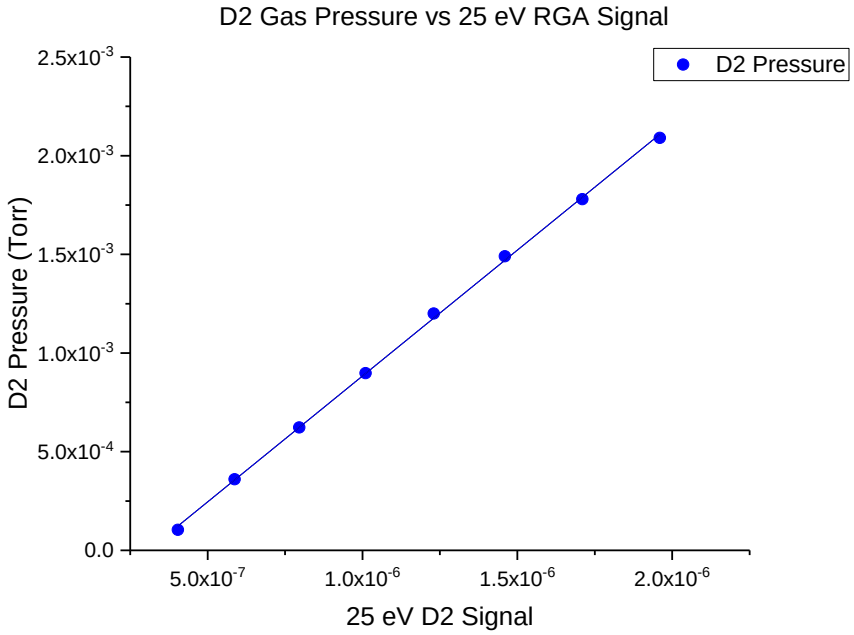

Figure 22. The true pressure of D_2 was measured using a CMR365 Pfeiffer Baratron Vacuum gauge and related to the signal measured by the RGA set to an electron energy of 25 eV.

In the situation where a sample is undergoing TDS, molecules will be desorbing off the surface, and the RGAs will measure the signal associated with the desorbed molecules. The 25 eV signal corresponds only to D_2, as seen in figure 21, so once measured, the 25 eV signal is converted into a pressure using the calibration curve in figure 22. Figure 22 used baratron pressure readings to ensure that the calibration was as accurate as possible. The calibration represents the pressure in the HIDRA-MAT main chamber due to D_2. As expected, the RGA signal increases with an increase in pressure due to more D_2 atoms reaching the RGA and being ionized.

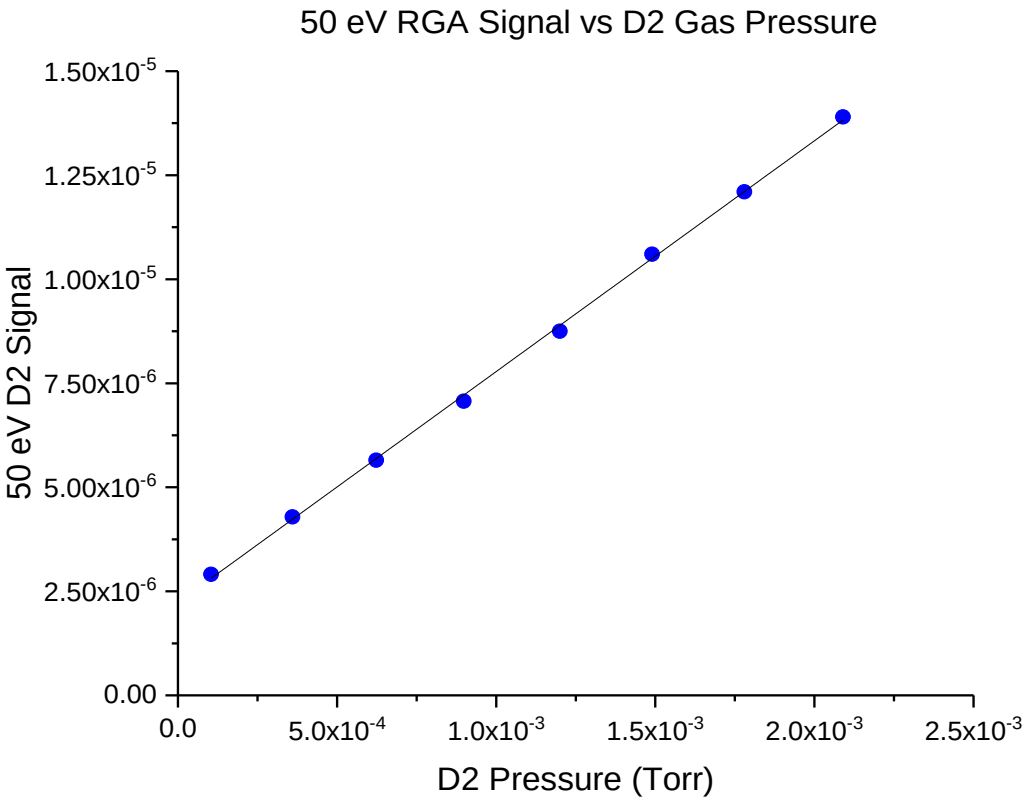

Figure 23. A linear fit relating true D_2 pressure to the signal measured by the 50 eV RGA

The physical D_2 pressure desorbing off the sample surface is now known and has to be compared to what the physical pressure from He desorbing off the surface would be to identify the gas mixture. Another calibration curve, helping convert D_2 pressure into a 50 eV RGA signal, is used and can be seen in figure 23. Once converted, the D_2 50eV RGA signal is subtracted from the

measured signal to calculate the amount of 50 eV signal that is due to He gas. This calculation is described in equation 2.

$$He\ 50\ eV\ Signal = (Measured\ 50\ eV\ Signal) - (D_2\ 50\ eV\ Signal) \quad (2)$$

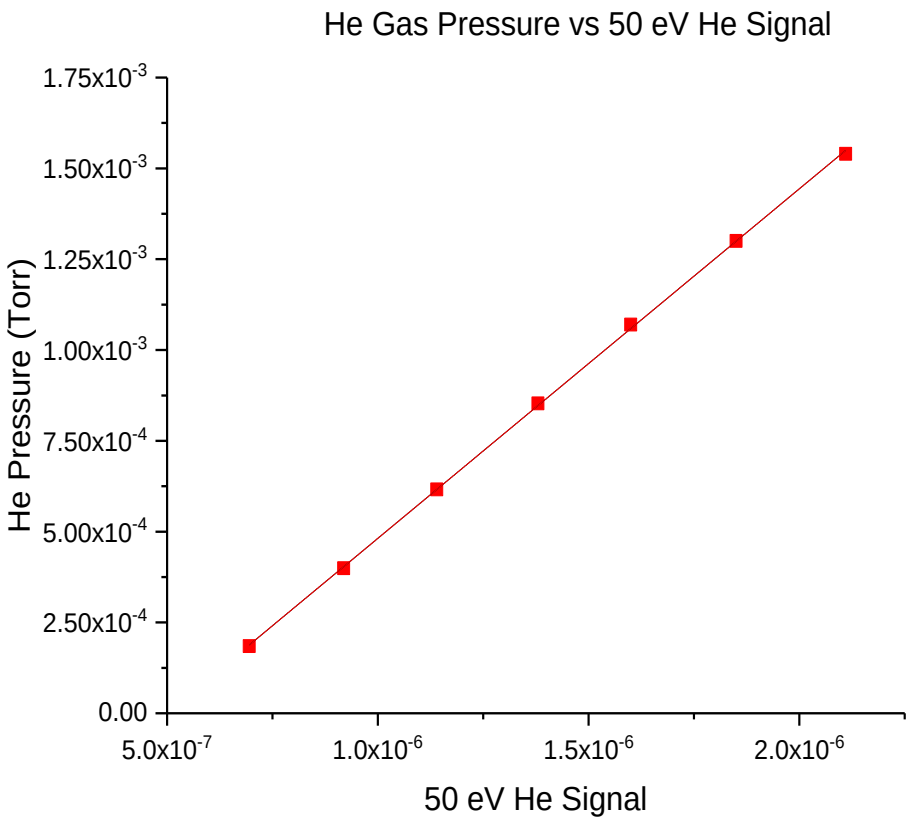

Figure 24. Flowing pure He gas into HIDRA-MAT produces a calibration curve relating the He signal measured by the 50 eV RGA to the true pressure in the HIDRA-MAT main chamber measured by the baratron.

The next step is to convert the He signal back into a physical pressure value. This is done by yet another calibration curve shown in figure 24. After this final conversion, there is now a physical gas pressure from both He and D_2 originating from the signals collected on the dual-RGA system. Equation 3 can then be used to determine the percentage of He to D_2, thus showing that the two gases with nearly identical gases can be differentiated and quantified into physical pressure values which, can be used in determining a sample's retention of each gas after plasma exposure.

$$\% He = 100\left[\frac{P_{He}}{P_{He} + P_{D_2}}\right] \quad (3)$$

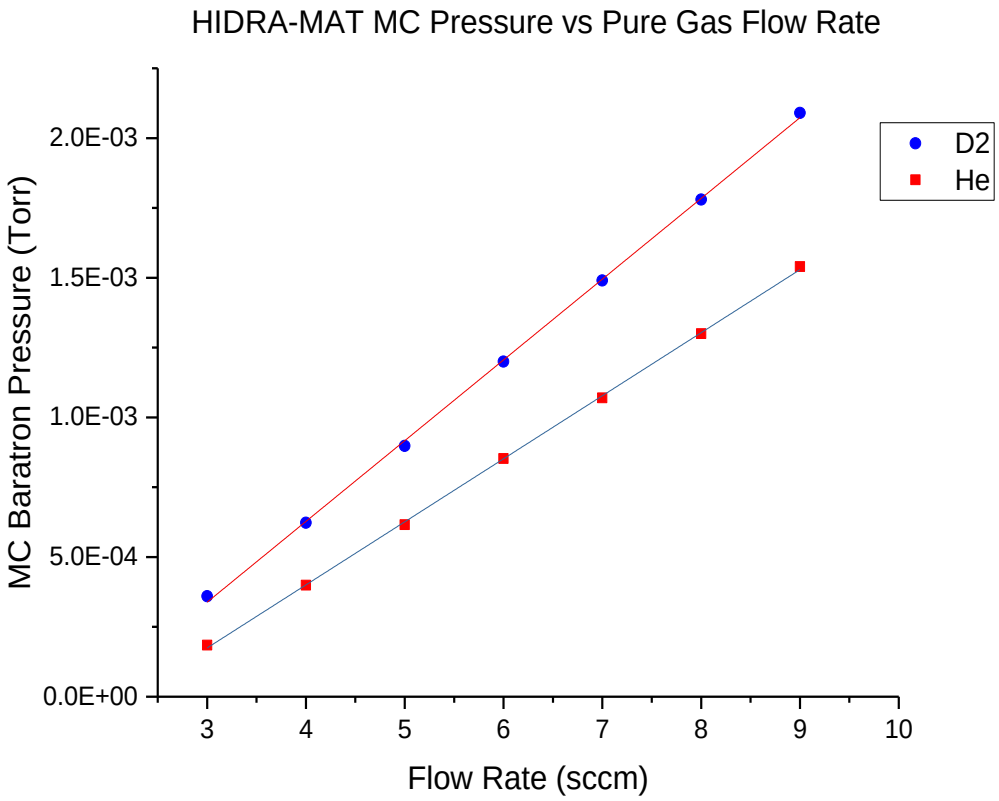

Figure 25. Differences between D_2 and He result in similar flow rates producing different pressures in the HIDRA-MAT main chamber. This data was used to determine MFC setpoints for different He:D_2 mixtures. Flow rates below three sccm could not produce a stable signal to be able to make an accurate pressure measurement.

The differentiation methodology has been presented, and the experimental results are to follow, demonstrating how well the system works in practice. To do so, data was collected on flow rates of pure He and pure D_2 gas that corresponded to pressures in the HIDRA-MAT main chamber measured by the baratron gauge. This data is presented in figure 25 and was used to determine the flow rates of each gas to create specific gas mixtures. The data shows that the same flow rates do not result in the same pressure in the HIDRA-MAT main chamber even though the gases are the same mass. Due to this, the linear fits created from figure 25 have to be used to determine what each gas' flow rate has to be to create the desired mixture. Relying on flow rates alone without the

data in figure 25 to determine mixture would lead to inaccuracies in the analysis of the dual-RGA system's effectiveness. The flow of gas was controlled using two SmartTrak 100 MFCs that are calibrated for ten different gases in which He and D_2 are included.

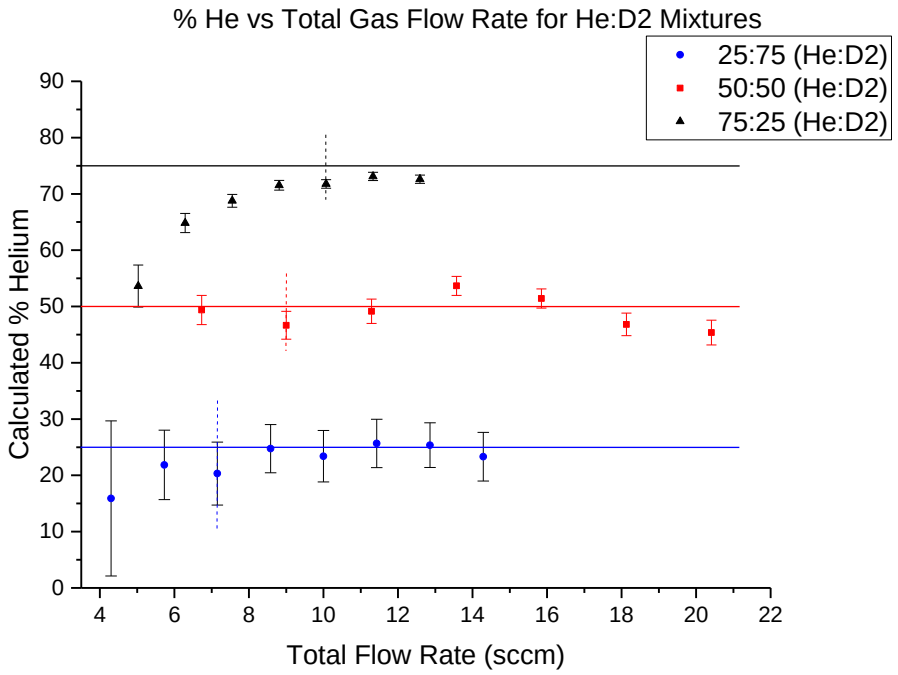

Figure 26. Total flow rate of the He:D_2 gas mixture versus the calculated He percent determined from the differentiation method. Three distinct He concentrations were attempted and are shown by solid horizontal lines. The differentiation method produced results that followed closely to the attempted mixtures. Dashed vertical lines act as a cutoff for data points where the flow rate of He or D_2 were outside the range of flow rates used in figure 25.

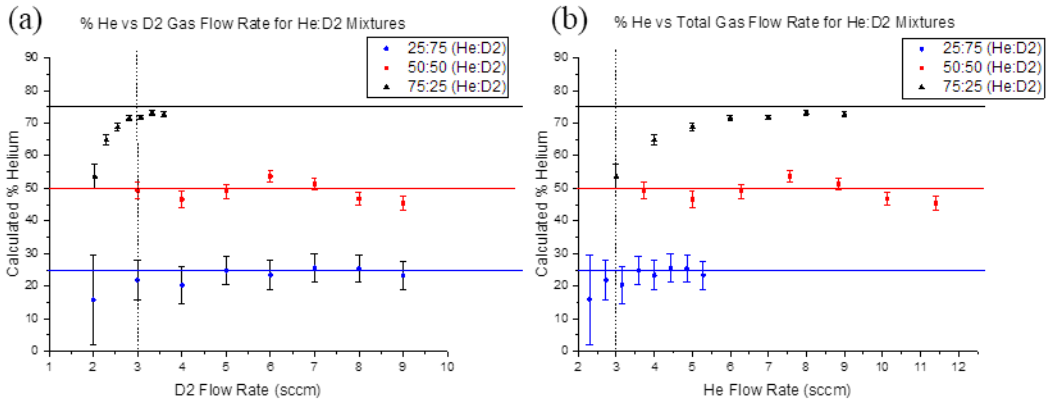

Figure 27. Flow rate of (a) D_2 and (b) He in He:D_2 gas mixture versus the calculated He percent determined from the differentiation method. Three distinct He concentrations were attempted and are shown by solid horizontal lines. The dashed vertical line in each figure act as a cutoff for data points where the flow rate of He or D_2 were outside the range of flow rates used in figure 25.

The data from testing the dual-RGA system with known gas mixtures are included in figure 26. It is important for the reader to understand that the "known gas mixtures" have an error associated with them through a multitude of factors, including potential error in the MFC, the linear fits in figure 25, and gas flow dynamics inside of HIDRA-MAT. The MFCs operate with a 1% tolerance, and the pressure measurements during the pure gas flow calibration have to be averaged over an extended period of time at pressure ranges at or below 10^{-3} Torr to collect accurate measurements. Below 10^{-4} Torr, the baratron gauge measurements cannot be used, and the linear fit is used to determine flow rate to pressure conversion. The three dashed lines in figure 26 represent the start of data points that both gas flow rates are at or above flow rates measured (the lowest pure gas flow rate measured that still gave accurate baratron pressure measurements was three sccm for each gas) in figure 25. Figure 27 shows the calculated He percentage as a function of each gas' flow rate into the HIDRA-MAT main chamber. A dashed vertical line on figures 27a and 27b indicates flow rates below the flow rates measured using the baratron gauge pressure measurement in figure 25 and thus data that relied solely on the fit of the data. Figure 27a reveals that the data is strongly dependent on the flow rate of D_2 when it comes to determining gas mixtures. This signals that there is most likely a change in the data at these low flow rates from a linear relationship to a non-linear one. Gas flow dynamics could play a role in explaining discrepancies in the data when looking at the desired gas mixture and the calculated gas mixture, specifically looking at low gas flow rates and higher percentages of He compared to D_2. There is confidence in the data's accuracy, and further explanation of error propagation in the calculated data will be discussed in the following section.

Overall, when flow rates of He and D_2 are both above three sccm, the gas mixture calculation better follows the expected gas mixture. Between the three gas mixtures investigated,

the He percentage followed closely to what was expected. The differentiation system was able to distinguish between the amount of He and D_2 in the system just from the dual-RGA signals with an error close to ±5% depending on the gas mixture. Baratron limitations at low pressures make it difficult to calibrate for differentiation, but it is seen that at higher flow rates, the system does relatively well. Future work on this system will address the lower flow rate issues and can potentially be solved by operating the differentiation system with the main chamber at a higher pressure that the baratron can be used and introducing a known leak.

6.3 Error Propagation

Error propagation calculations have been done and included in figures 26 and 27. The error bars are tolerable, showing less than ±5% error for the majority of data points establishing confidence in the method. Identifying the largest sources of error in the measurement provide insight into how the measurement can become more accurate. The percentage of He compared to D_2 is the final calculated value shown in figures 26 and 27. This value is obtained from equation 3, and its standard deviation, Δf, is calculated from equation 4.

$$\Delta f = \sqrt{\left(\frac{\partial f}{\partial P_{He}}\right)^2 (\Delta P_{He})^2 + \left(\frac{\partial f}{\partial P_{D_2}}\right)^2 \left(\Delta P_{D_2}\right)^2} \qquad (4)$$

Equation 4 is dependent on the standard deviation associated with the pressure calculation of He (ΔP_{He}) and D_2 (ΔP_{D_2}). The contribution each source has towards the overall error is included in table 5 for each mixture, which can be found in Appendix B along with the rest of the calculations regarding error propagation. This data shows that the calculation for the error associated with the He percent calculation relies heavily on the calculation of the ΔP_{He} term. This dependence is more pronounced for He:D_2 mixtures with low percentages of He. Each term in the percentage

calculation, $\left(\frac{\partial f}{\partial P_{He}}\right)^2 (\Delta P_{He})^2$ and $\left(\frac{\partial f}{\partial P_{D_2}}\right)^2 (\Delta P_{D_2})^2$, is a product of previous calculations using linear fits on the data shown in figures 22-24 in section 6.2. Following error propagation through the differentiation methodology will explain what steps are most likely to introduce error.

The standard deviation for the calculation of the physical pressure of D_2 gas is shown in equation 5. The standard deviation of the slope, Δm, and the intercept, Δb, are produced with the fit of the line in figure 22. The 25 eV measured signal has an associated standard deviation as well and can be calculated from the gas mixture data sets using equation 6. Each value from the population, the population mean, and the size of the population are denoted by $x_i, \mu,$ and N respectively. The non-zero term contributions for ΔP_{D_2} can be found in table 6. The product of the standard deviation and derivative $\left(\frac{\partial P_{D_2}}{\partial b}\right)^2 (\Delta b)^2$ will be zero because of the linear fit. Additionally, standard deviations for both the 25 eV measured signal, Δx, and 50 eV measured signal, Δw, have been presented in table 7. Looking at the term contribution from equation 5 it is clear that the majority of the error is contributed from the measurement of the 25 eV signal, and that is expected as long as there is confidence in the conversion from RGA signal to the actual pressure. To reiterate, there will be a small amount of error associated with baratron measurements, but the only data points used in the linear fits were stable pressure readings from the baratron.

$$\Delta \mathrm{P}_{\mathrm{D}_2} = \sqrt{\left(\frac{\partial P_{D_2}}{\partial m}\right)^2 (\Delta m)^2 + \left(\frac{\partial P_{D_2}}{\partial x}\right)^2 (\Delta x)^2 + \left(\frac{\partial P_{D_2}}{\partial b}\right)^2 (\Delta b)^2} \tag{5}$$

$$\Delta x = \sqrt{\frac{\Sigma (x_i - \mu)^2}{N}} \tag{6}$$

Now focusing on the ΔP_{He} term, the main source of error in the mixture calculation, can be calculated using equation 7. The standard deviation of the slope, Δl, and the intercept, Δc, are

produced with the fit of the line in figure 24. The standard deviation of the 50 eV He signal, Δz, contributes the most amount of error, found in table 8, independent of total flow rate or gas mixture, and is found using equation 8. Equation 8 follows a different form than the other standard deviation calculations because the 50 eV signal is found from equation 2 rather than a conversion, which uses a linear fit of data points. Table 9 shows that the term contribution is relatively equal, with the 50 eV signal measurement term contributing slightly more to the overall error. Since these two terms provide similar error contribution, equation 9 has been included to follow the source of error in Δy, the calculation of the standard deviation of the 50 eV D_2 signal. Table 10 shows that the ΔP_{D_2} term contributes all the error, and relating that back to term contribution in equation 5, it is known that the measurement in the 25 eV signal contributes most of the error to that calculation.

$$\mathrm{P}_{He} = \sqrt{\left(\frac{\partial P_{He}}{\partial l}\right)^2 (\Delta l)^2 + \left(\frac{\partial P_{He}}{\partial z}\right)^2 (\Delta z)^2 + \left(\frac{\partial P_{He}}{\partial c}\right)^2 (\Delta c)^2} \tag{7}$$

$$\Delta z = \sqrt{(\Delta w)^2 + (\Delta y)^2} \tag{8}$$

$$\Delta y = \sqrt{\left(\frac{\partial y}{\partial n}\right)^2 (\Delta n)^2 + \left(\frac{\partial y}{\partial P_{D_2}}\right)^2 \left(\Delta \mathrm{P}_{\mathrm{D}_2}\right)^2 + \left(\frac{\partial y}{\partial a}\right)^2 (\Delta a)^2} \tag{9}$$

With all this said, the error propagation study yielded the expected results that the error in the mixture calculation comes from the measured RGA signals. It is important to identify this source of error because it highlights the factors in the differentiation method that can be improved upon. To obtain more accurate results, the accuracy of the RGAs would have to be improved. This can be achieved by taking more data points at specific flow rates, using longer data sets to improve accuracy, or purchasing more accurate RGA systems.

Chapter 7: Laser-Induced Breakdown Spectroscopy

7.1 LIBS Background

LIBS is emerging as a popular characterization technique across many scientific disciplines, one of which is fusion materials. Single-pulsed LIBS (SP-LIBS) utilizes a focused, high-energy laser pulse onto a sample to form a localized plasma above its surface. Plasma formation is achieved by first ablating the material on the sample's surface with the laser's pulse. Ablated material will form a plume of ejected material normal to the surface. With an incident laser angle normal to the sample surface, the beam will interact with the ablated material it has. The ejected ablated material becomes ionized and creates a plasma. As the plasma forms, plasma shielding will cause the laser beam's energy to be deposited into the plasma rather than the material [25]. Higher laser energy will yield more ablated material and a stronger plasma.

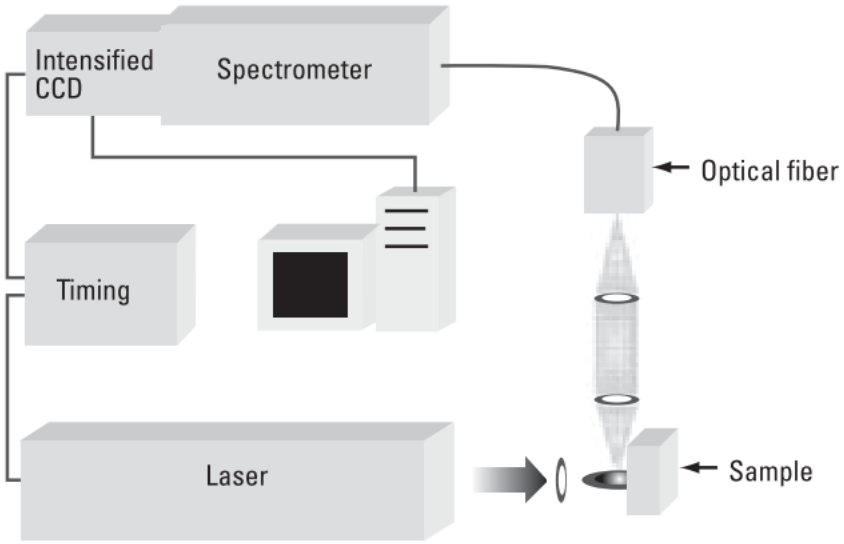

Figure 28. SP-LIBS setup using an ICCD camera with the spectrometer collecting light from aa 90° angle with the AOI of the beam *[41]* .

The experimental setup dictates the specifics of the LIBS setup. Laser type becomes the first thing to consider, followed by the geometry of laser optics, sample, and collection optics, sample

material, and timing controls when constructing a LIBS setup. Nanosecond pulsed Nd:YAG lasers are typically used in these setups because of their ability to produce high energy pulses with harmonics at 1064 nm, 532 nm, and 266 nm. Laser energy required is dependent on if the sample material that is being characterized is a solid, liquid, or gas. The next consideration in a LIBS setup is the geometry of laser, sample, and collection optics.

In most cases, the laser beam is normal to the sample surface to maximize the interaction between the beam and ablated material. However, research investigating signal variation spatially in the plasma plume has utilized different sample-laser angles and observation angles [26, 27]. Collection optics are generally at a low angle with respect to the incident laser beam or collinear with the incident laser beam. In collinear LIBS setups, dichroic mirrors are implemented to direct the beam towards the sample while simultaneously allowing light from the plasma to pass through to be collected. Collection optics can also be positioned 90° to the plasma plume, as seen in figure 28.

LIBS plasma formation must be understood to grasp the meaning of the signal that is being obtained. Plasma formation is dependent on either thermal or non-thermal effects at the material surface. Non-thermal effects arise if femtosecond lasers are used, while thermal effects are dominant if a nanosecond laser is used. In femtosecond pulses, thermal effects do not have enough time in the pulse to evolve fully, so the dominant mechanism is a Coulomb explosion. Nanosecond pulses have a longer timescale for thermal effects to fully develop and become the driving mechanism for plasma formation. The heating and melting of the substrate lead to ablation and ionization of the material. The crater left behind from a nanosecond pulse is deeper into the substrate. The crater's edges are less defined than craters created from the femtosecond pulse because of the melting in the material lattice. The advantage of the nanosecond pulse is the

occurrence of plasma shielding that reheats the plasma. The plasma develops to a point where it prevents the laser irradiance from passing through and ablating the substrate, and instead, all of that power is now delivered to the plasma. This plasma shielding extends the lifetime of the plasma [25]. The plasma's properties, such as electron temperature and density, rely on the amount of ablation, laser energy deposition, environmental factors (pressure, gas species), and more. In a vacuum, the plasma adiabatically expands and cools after it has interacted with the laser pulse. The scope of this work covers nanosecond laser pulses under vacuum conditions. Atomic emission occurs during the cooling of the plasma, and the optical fiber collects the emitted light. This light creates the LIBS spectra and provides information on the composition of the sample's surface.

HIDRA-MAT will use LIBS on fusion PFCs, and most fusion PFC's incorporate W as the main part of their design with liquid metal PFCs. Adding to the complexity of designing fusion PFCs are the particles they interact with from the plasma. With LIBS being sensitive to sample material, Li and W's LIBS signals were crucial to this work. Table 1 contains the known emission lines correlated to Li, and W. H and D have few emission lines because hydrogen and its isotopes have one electron. A W atom has 74 electrons and thus many more spectral lines. The lines in the table are the lines identified in literature examples that most closely follow the experimental conditions in HIDRA-MAT [28, 29, 30, 31, 32].

Table 1. Main emission lines from $H_\alpha, D_\alpha, Li\ (I), Li\ (II), W\ (I)\ and\ W\ (II)$.

Name	Main Emission Line(s) (nm)
H_α	656.279
D_α	656.092
Li (I) (Neutral)	610.365, 670.811
Li (II) (Ionic)	548.428

Table 1 (cont.)

Name	Main Emission Line(s) (nm)
W (I) (Neutral)	429.4, 451.2, 656.32, 656.779, 657.393, 658.291, 660.905, 661.162, 662.064
W (II) (Ionic)	434.81

The H_α and D_α peaks communicate important details about the PMI during plasma discharges. H_α will be present in experimental samples from the absorption of water. The disassociation of water molecules during LIBS will give rise to the H_α peak. This peak will be more prominent if hydrogen gas is being used in the experiment. The D_α peak resides less than 2 Å from the H_α peak and part of the WI peak overlaps with the H_α peak requiring spectrometers with high resolutions to be used to discern the peaks from one another. With all these peaks within angstroms of one another, the signal strength becomes the main constraint on data collection next to spectrometer resolution. The main avenues of increasing signal strength are changing laser energy, spectrometer delay times, or chamber pressure. Background gases are often used to improve the plasma's signal strength because the ablated material collides with the gas and can ionize more of the ablated material. In contrast, when no background gas is present in the vacuum, the plasma can freely expand, and plasma shielding effects are less intense [29]. Experiments involving LIBS with a Mo and W at different air pressures saw no change in line intensity at pressures of 10 Pa and below. There was an increase in line intensity with pressures higher than 10 Pa with the peak intensity around 3×10^4 Pa followed by a sharp drop off [32, 33]. Delay times between laser shot and spectrometer acquisition start time. The delay time is unique to each LIBS setup, but numerous experiments have reported optimized delay times in the range of 100 ns - 3 μs across a variety of experimental conditions on fusion PFC materials [29, 32, 34, 35].

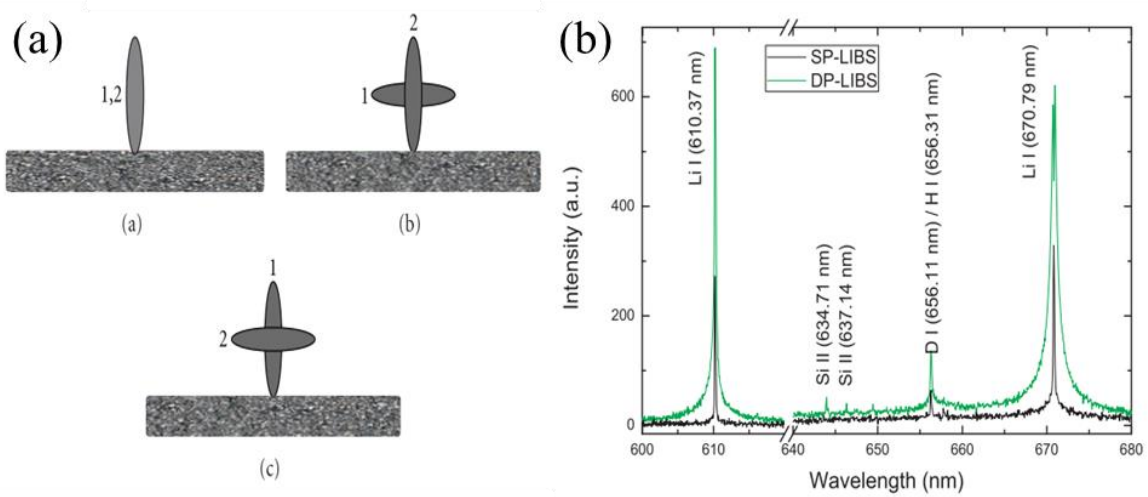

Figure 29. Different geometries for (a) both pulses of a DP-LIBS configuration *[25]*. HIDRA-MAT will implement a collinear pulse. Signal strength for (b) DP-LIBS compared to SP-LIBS *[32]*. DP-LIBS sees a dramatic increase in signal.

Laser energy has a substantial effect on the intensity of the signal. Larger energies will be able to ablate and ionize more material resulting in a stronger signal. More ablation will cause a deeper crater to form, enhanced melting at the crater's edges, and more overall damage to the surface. If analysis based on depth was considered, lower laser energy can provide better depth resolution with each LIBS pulse since crater depth would be reduced. The LIBS plasma lifetimes are on the order of a microsecond giving a justification as to why the signal is so low. ICCD detectors, image intensifiers, and nanosecond gate windows have all been employed to reduce noise and enhance the signal. An alternative option that was developed following the early success of SP-LIBS was dual-pulsed LIBS (DP-LIBS). The observed phenomenon of plasma shielding and laser energy deposition led to the development of DP-LIBS to increase the plasma signal. Introducing the second pulse into the opaque plasma helps increase the ionization of ablated material without ablating more material. The results are a longer LIBS plasma lifetime, which directly correlates to a more intense signal. DP-LIBS experiments found optimum laser pulse delays between $.5 - 2\ \mu s$ [27, 32]. This spacing is achieved either by separating a single beam using optics or using two lasers timed off a delay generator.

Figure 29a describes how the beams are conventionally used in a collinear or orthogonal orientation to maximize laser energy deposited into the plasma. Results from multiple experiments performing LIBS on fusion PFC materials showed a substantial increase in signal when DP was employed over SP methods, as seen in figure 29b. This figure also demonstrates spectra that were obtained using similar equipment on HIDRA-MAT, which is shown and discussed later in this chapter.

The difficulty associated with characterizing fusion PFCs comes with their associated environment. *In-situ* characterization requires minimally invasive techniques that also can be achieved in high-vacuum conditions. Typical methods involve samples being exposed to atmosphere, which introduces surface changes due to oxidation and other potential impurities.

7.2 HIDRA-MAT LIBS Original Experimental Setup

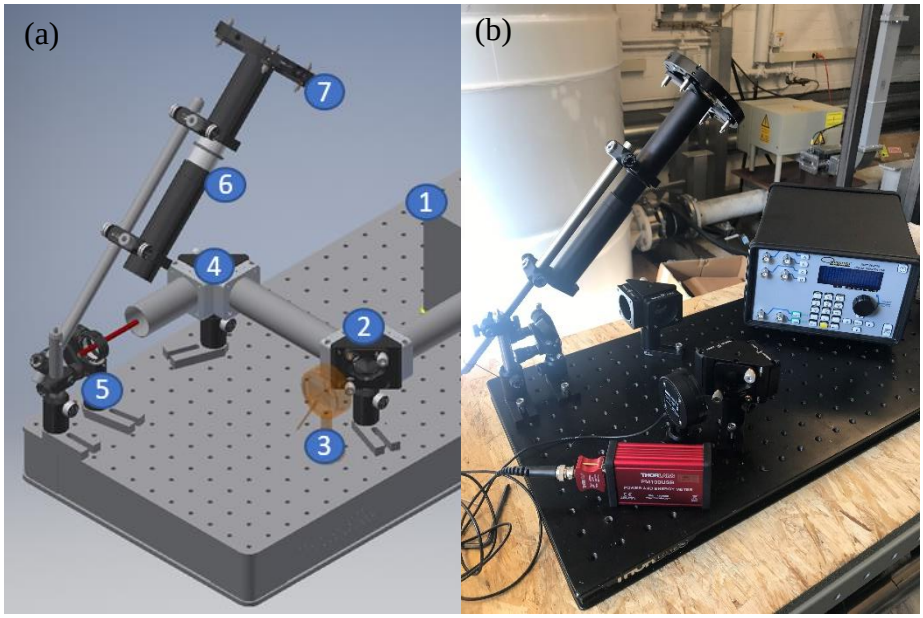

Figure 30. The (a) CAD of a fully assembled LIBS system with the following labeled components: (1) 532nm Nd:YAG laser (2) 90:10 (R:T) UVFS plate beamsplitter (3) ES220C pyroelectric energy sensor (4) Nd:YAG mirror (5) gimbal mount, 360° adjustable with Nd:YAG mirror (6) adjustable lens tube and lens (f=500mm) and (7) transmission viewport. Assembled (b) LIBS optics along with pyroelectric sensor and pulse generator before they were installed onto HIDRA-MAT.

The original LIBS system design, shown in figure 30, includes a Litron B-PIV 532 nm nanosecond pulsed laser with a pulse energy of 145 mJ at 15 Hz. The laser can be operated in both

SP and DP modes. Optics redirect and focus the beam to a spot size of ~1 mm, resulting in a calculated power density of 4.15×10^{12} W/m^2 at maximum pulse power, consistent with similar LIBS experiments on tungsten PFCs [17]. The plano-convex focusing lens is coated with a 532 nm optical coating to reduce the beam's transmission loss. The position of the lens can be adjusted through an adjustable lens tube. The laser can separate the two pulses within $.5 - 2\,\mu s$ of each other from programmable settings on the laser's user interface. The first pulse will produce the ablation of the sample material. The second one can be triggered after an optimized delay that maximizes the eventual plasma plume formation and the concomitant spectral emission from the ablated and exciting material. After the dual pulse, a Quantum Composers 9520 Series pulse generator will trigger two Ocean Insight HR2000+ series spectrometers to collect and analyze the light signal. As noted before, the delay between laser and spectrometer trigger is sensitive to each specific LIBS setup and will range from hundreds of nanoseconds to microseconds. The first spectrometer ranges from 200 nm to 1100 nm and will scan a range of wavelengths that include Li, W, and any other contaminants' peaks with a 0.1 nm resolution. The second spectrometer ranges from 630 nm to 680 nm and can resolve the H_α and D_α peaks present with a resolution of 0.2 Å. Future experimental campaigns will strive to quantify retention in samples.

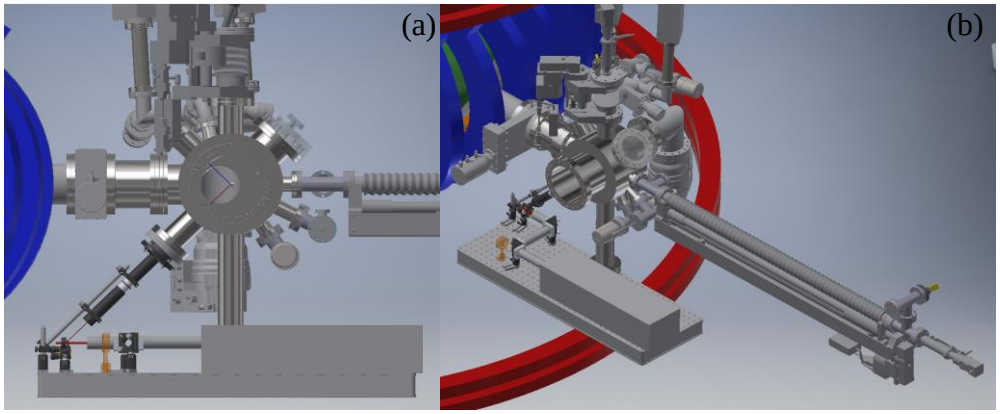

Figure 31. CAD of original HIDRA-MAT LIBS design from a (a) side-view showing the 45° AOI from both the beam and spectrometer with respect to the sample and (b) ISO-view showing how the LIBS systems is places with respect to the rest of HIDRA-MAT and HIDRA.

The laser and optics are positioned below HIDRA-MAT attached to an optical breadboard. The beam path first interacts with a 90:10 (R:T) beamsplitter. The transmitted beam hits an ES220C pyroelectric sensor, which measures the beam energy. The sensor can resolve nanosecond pulses to measure beam energies in both SP and DP-LIBS scenarios. The reflected beam is directed towards a mirror that reflects it 90° towards another mirror in a gimbal mount. The gimbal-mounted mirror reflects the beam at a 45° angle through the lens tube and into the HIDRA-MAT vacuum chamber. The Nd:YAG plano-convex mirror focuses the beam through an Nd:YAG quartz laser transmission viewport specifically made to maximize the 532 nm beam transmission before hitting the sample. The entire beam path is either enclosed or covered by blackout material from leaving the laser to hitting the sample.

The sample's initial placement was horizontally positioned and 45°AOI with the beam depicted by figure 31a. The reason for this placement was for simplifying beam alignment and reducing a source of error for the sample to have to be rotated if not necessary. The direct line of sight of the fiber optic connection to the sample was 90° with respect to the beam's AOI.

7.3 First Results with LIBS and LIDS

The first LIBS experiment was conducted on the porous tungsten sample that was part of the LMDI test. For simplicity in understanding the LIBS system, an SP approach was chosen to avoid needing to attribute time towards the optimization of inter-pulse delay. The sample was brought up to atmosphere after the liquid metal droplet was applied to align the beam correctly. Bringing the sample to atmosphere undoubtedly introduced the surface's passivation but did not affect the anticipated experimental results. As an addition to the experiment, an RGA was added to the HIDRA-MAT main chamber to perform laser-induced desorption spectroscopy (LIDS). The ablated material will be ejected into the chamber, and the RGA will measure the partial pressures

for each pulse. In tandem with the spectroscopy results and 3D profiling of the surface, quantification of LIBS signals can potentially be made.

Following alignment, the chamber was pumped down to 2.64×10^{-7} Torr. The initial delay of the spectrometer acquisition to laser Q-switch pulse was 500 ns. The integration time on the spectrometer was at its minimum value of 1 ms. The laser pulse energy was set to 80%, which resulted in an averaged measured pulse energy at the pyrometer of 14.34 mJ. Assuming no losses, the average beam energy at the sample over the 14 shots was 129.09 mJ. Using an estimated 2 mm spot size, the power density at the sample was 5.13 W/m^2. Over the course of the 14 shots, no usable LIBS spectrum was found. The lack of signal was attributed to a few factors, the first of which was laser and fiber optic geometry. The ablated material will eject normal to the surface irrespective of the laser's incidence, and the area of the plume the laser interacts with is reduced the more the AOI deviates from normal to the surface. Experimenting with low pressure allowed the ablated material to freely expand with negligible effects from collisions with the surrounding environment. The combination of beam AOI and free expansion of ablated material are probable factors for the absence of signal. Additionally, inspection after the LIBS shots showed that the sample had not been hit. An unknown source of misalignment had the beam hit the sample clip holding sample.

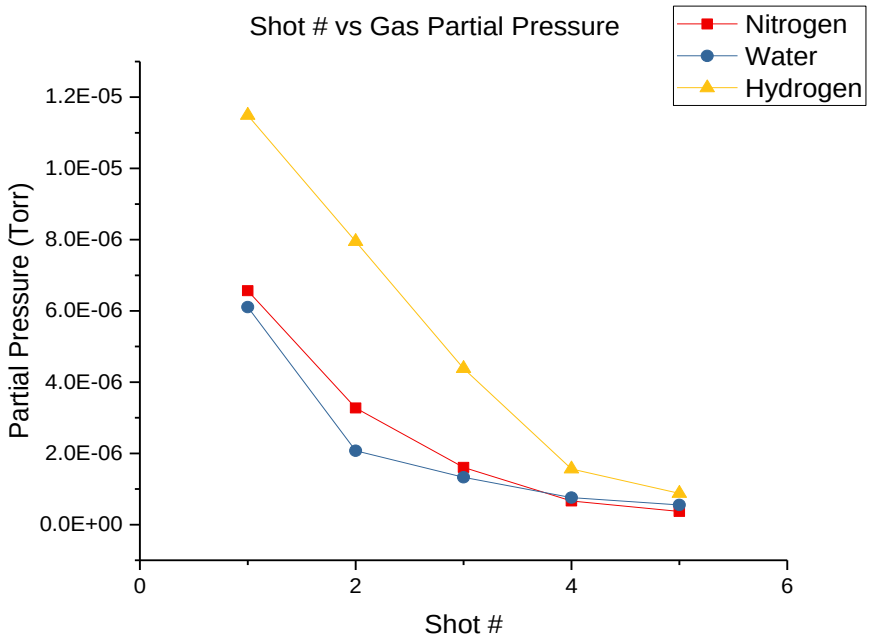

Figure 32. Partial pressure data of H, N_2, and H_2O from the first 5 LIBS shots at a pulse energy of ~128 mJ. Partial pressure decreases with each shot as oxides and water are removed from the surface.

The laser pulses hitting the aluminum sample clip prevented any LIBS sample data from being collected but did produce LIDS data. The RGA monitored specific masses of common gases during the LIBS pulse, and the increase in partial pressures could identify each pulse. Taking peak partial pressure values from the RGA data, figure 32 shows the decrease in peak intensity as the laser pulses ablate more material off the clip's surface. After the first 3 LIBS shots, the RGA was set to only monitor hydrogen, nitrogen, and water to increase the resolution of the data.

7.4 Secondary HIDRA-MAT LIBS Experimental Setup

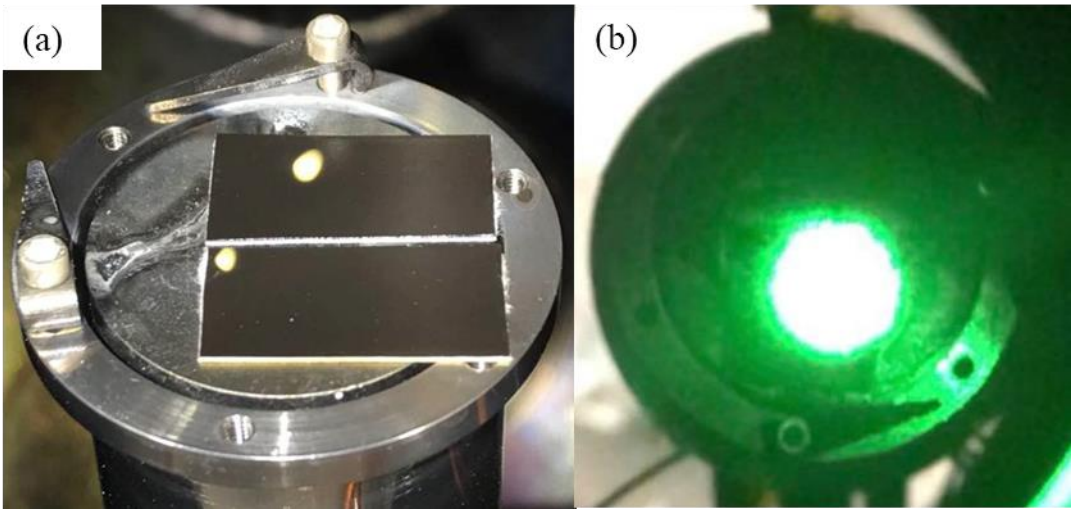

Figure 33. LIBS (a) laser spot alignment using light sensitive laser paper and (b) collection optics alignment. Precise alignment is vital to obtaining the maximum LIBS signal possible.

After the first LIBS experiment, stark changes needed to be made to increase signal strength. The sample is now rotated 45° from the horizontal position such that the beam AOI is normal to the sample surface. The new AOI ensures that the laser pulse will be deposited entirely into the plasma rather than deposited into a small section. The increased power deposition into the induced plasma should lead to a stronger signal captured by the collection optics and spectrometer. An advantage of rotating the sample is that all rotation for diagnostic characterization (LIBS, TDS) and sample preparation (droplet application) can be done from the transfer arm's same linear position. The line of sight from the 8” side window is taken away, so alignment is now done using the 2.75” transmission window. Pictures for laser spot and collection optics in figure 33 give an idea of how alignment is verified.

7.5 Results of Second LIBS Experiment

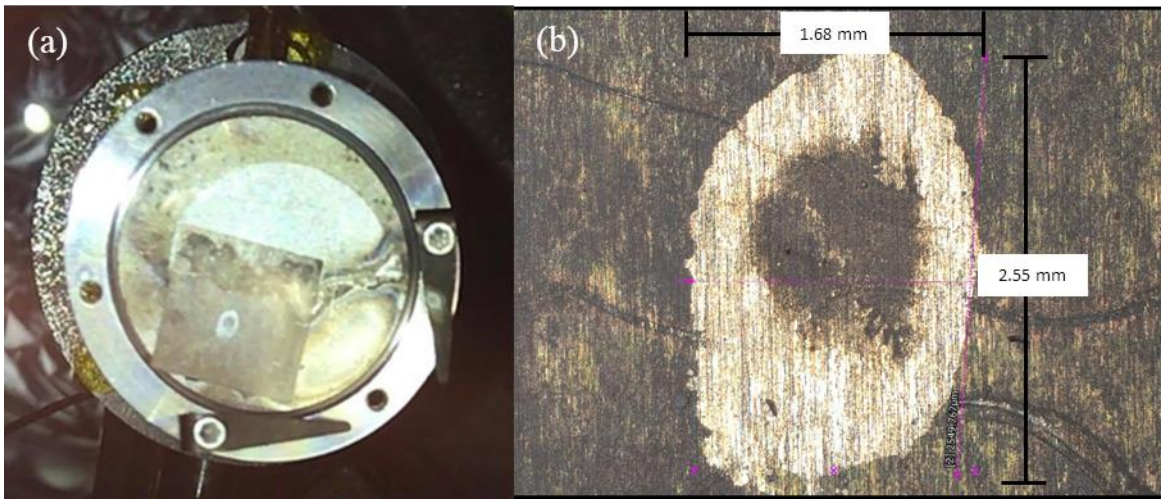

Figure 34. A LIBS laser pulse of ~123 mJ left an ablation mark on (a) a lithiated tungsten foil sample in HIDRA-MAT. The (b) ablation mark was imaged using a Keyence VK-X1000 to measure feature sizes [Credit: Alfonso de Castro]

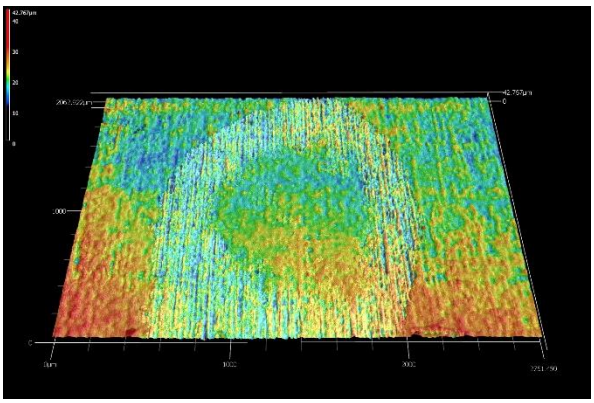

Figure 35. 3D-profilometry of the lithiated tungsten foil sample's surface roughness. The beam energy was more concentrated on the outside of the beam leaving it difficult to know the crater depth on the rough surface (1.8 μm). The beam must be focused better in order to ablate material, create a crater and plasma, and obtain a LIBS signal [Credit: Alfonso de Castro]

The second set of LIBS experiments on HIDRA-MAT illustrated that more modifications to the LIBS design were necessary. The sample used was a lithiated piece of tungsten foil. The laser pulse hit the sample, and the effect of that pulse on the sample's surface is seen in figure 34a. When observed with the Keyence VK-X1000, the images show the pulse's energy deposition was concentrated on the outer edge shown in figure 30b, and depth profiles confirm that fact in figure 35. The focusing lens used had a focal length of 500 mm, and the sample was placed 300 mm from

the lens. The lack of focusing and divergence effects caused the spot size to be 2.55 mm in length and 1.68 mm in width.

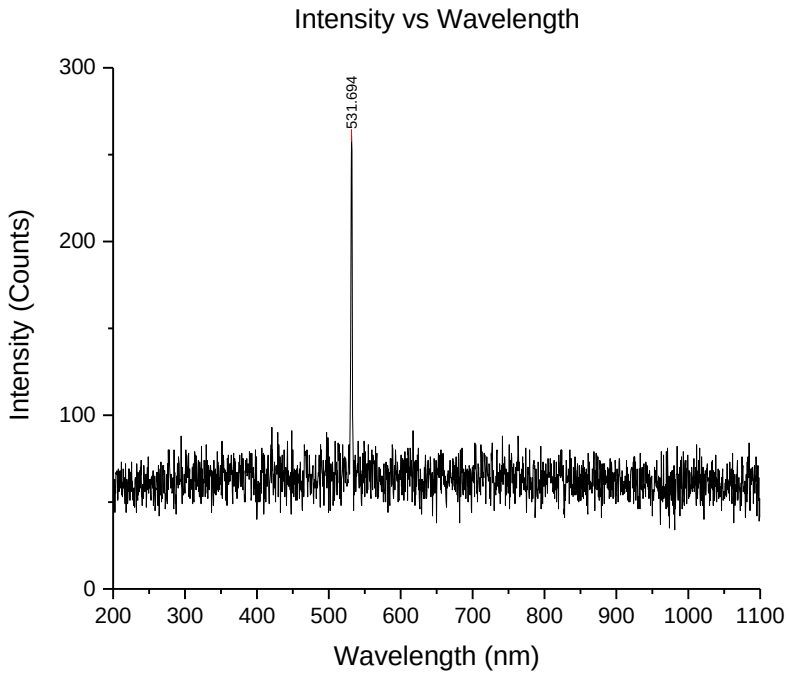

Figure 36. Spectrometer signal showing the reflection of the 532 nm laser light.

Though the collection optics were aligned, the spectrum collected did not show the presence of lithium or tungsten. The spectrum only captured a sharp peak at 532 nm, shown in figure 36, corresponding to the wavelength of the laser. Reflection of the laser light off the sample heater is expected, but a short-pass filter could be implemented to direct expected signal wavelengths into the optical fiber while avoiding signal saturation from the laser light itself. Secondly, the laser's energy deposition at the surface was most likely not enough to produce enough ionization in the plasma for a signal to be collected. A focusing lens with a shorter focal length can be installed to remedy this, so the beam is focused on the sample. Energy deposition into the induced plasma will then be more efficient, and the increased ionization effects will produce a stronger signal.

7.6 Results of Third LIBS Test

The third LIBS test set out to expand on the previous test and produce a LIBS spectrum. A new focusing lens (f=300) replaced the previous focusing lens (f=500) to reduce spot size with the beam's energy focused in the center of the beam rather than the outside of the beam profile. Alignment at different lens positions (270-330 mm) from the sample yielded little to no difference in the beam spot size on photosensitive paper. Ultimately a lens position 280 mm from the sample was used for these tests, and more work has to be done to reduce spot size. The lithiated tungsten foil used in the second LIBS test was reused as the sample.

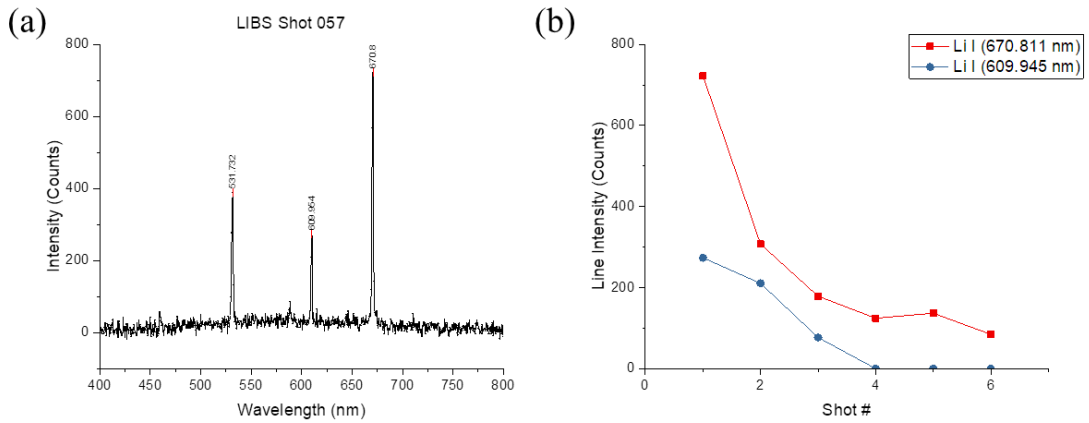

Figure 37. A (a) LIBS spectrum showing the Li I lines (~671 nm & ~610 nm) and the ~532 nm line (laser) after a ~179 mJ pulse at 76 Torr with a spectrometer integration time of 1 ms. Multiple shots (b) at the same sample location showed the lithium line intensity reduced as the laser penetrated deeper into the sample.

With a more focused laser spot, a series of LIBS shots were done at a chamber pressure of 76 Torr. This pressure had shown high LIBS line intensities in other experiments and was chosen to give the best opportunity to obtain a signal [32]. Even though the laser is rated for 145 mJ, the pyroelectric sensor registered a beam energy of 20.92 mJ. Factoring in losses from the beamsplitter and subsequent optics, the pulse energy was ~179 mJ. A built-in attenuator can reduce the beam energy, but the highest possible energy was preferred for this experiment. Figure 37a shows the LIBS spectrum obtained from hitting the sample and collecting the light with the HR2000+ 200-1100nm range spectrometer. There were three peaks present in the spectrum, and after calibrating

the line signals, the peaks were at ~532 nm, ~610 nm, and ~670 nm. The 532 nm peak reflects the laser light off the sample and UHV heater back to the collection optics. The 610 nm and 670 nm lines correspond to known Li I lines from figure 29b, signaling that lithium is present on the sample's surface as expected. Figure 37b highlights the LIBS system's depth profiling capability, showing the lithium line intensities decreasing with every shot. There were no observed tungsten, D_α, or H_α peaks in the spectra collected from either spectrometer (200-1100nm or 630-680 nm) either due to lack of signal strength or background continuum radiation, which would require light to be polarized before being collected [33].

It is promising that LIBS signals can be obtained in HIDRA-MAT, but more work still needs to be done to optimize the system. The pressures these spectra were collected at are too high; for accurate *in-vacuo* analysis, pressures will need to be at 10^{-6} Torr to avoid passivation of the sample's surface. A group of shots was performed on a new sample location at a pressure of 1 mTorr, and a lithium signal could only be from the first shot and was at a low line intensity. Low line intensities are expected in vacuum conditions because the ablated material has a larger mean free path before colliding with neutral gas particles around the sample surface. Observation of the sample post-LIBS did show that while the spot size of the beam has decreased in size, the beam was not fully focused, with the majority of the beam energy concentrated on the outer profile of the beam. Potential solutions to the low signal problem are introducing a background gas such as argon into the chamber during LIBS, continuing to troubleshoot the focusing issue of the beam, and adding a delayed second pulse to enhance the signal of the laser-induced plasma, otherwise referred to as DP-LIBS. Overall, with this experiment, the baseline functionality of HIDRA-MAT LIBS has been demonstrated, and future improvements will continue to enhance the signal.

7.7 Planned Experiments for HIDRA-MAT LIBS

LIBS on HIDRA-MAT will be utilized to collect data on the temporal evolution of the PFC's surface *in-vacuo*. Simulations have shown that in a 26 kW heating scenario operating at a low field (87.5 mT), HIDRA's poor plasma confinement gives rise to large particle fluxes to the sample on the order of 10^{22} $m^{-2}s^{-1}$. The stellarator pulse is on a much larger time scale than other devices, so many particles are interacting with the wall in one pulse. HIDRA-MAT studies the effects of these plasma characteristics by performing LIBS on exposed PFC materials. Since the plasma is still present in HIDRA when LIBS is being done in HIDRA-MAT, it can once again be exposed and then characterized. Combining separate LIBS measurements will elucidate the temporal evolution of how the PMI mechanisms are affecting the PFC.

With the sample being heated and lithium's high surface tension, lithium will remain a liquid and stay on the sample surface during the plasma exposure and characterization. LIBS can be performed on solids, liquids, or gases, making it advantageous for this application. In HIDRA-MAT's first experimental campaign, its dual-pulsed LIBS system will attempt to produce a strong signal depicting the retention of H, D, and He on the surface of lithiated porous tungsten that was exposed to a D-He plasma. Once *in-vacuo* characterization is complete, samples can be transferred out of HIDRA-MAT to other characterization diagnostics. The transfer will cause the sample to be exposed to atmosphere, immediately causing the surface to oxidize. Conclusions reliant on data from these secondary characterization techniques must take oxidation effects into account. The LIBS laser pulse will form a crater on the surface from ablated material, which will be measured with atomic force microscopy. Knowing crater depth opens the possibility of using multiple laser pulses and the signal obtained from each at the same sample location to produce a depth profile. Scanning electron microscopy imaging can be utilized to show crater location on the sample

surface, and 3D profilometry can characterize the crater's morphology to obtain metrics that will be useful to determine surface/volumetric retention values.

In-vacuo measurement is crucial to successfully identify liquid metal PFC behavior in fusion devices for H, D, and He retention. Characterization requiring samples to be taken out of vacuum immediately introduces impurities in oxidation and other atmospheric contaminants [36]. Lithium oxidizes quickly in atmospheric conditions, so *in-vacuo* characterization is a necessity. HIDRA-MAT and LIBS can gather the essential preliminary data on how these ions react with liquid lithium PFCs. *In-vacuo* characterization produces data that more accurately imitates realistic reactor conditions by removing external surface degradation.

Chapter 8: Conclusion

The development of HIDRA-MAT allows for PMI studies in a unique PFC testing environment. Stellarator plasmas, HIDRA's flexible experimental schedule, and HIDRA-MAT's versatile diagnostic setup allow various PMI experiments to be conducted. Within this work, the design, fabrication, and preliminary testing of HIDRA-MAT and its systems were presented. HIDRA-MAT's compact design features TDS, LIBS, and dual-RGA systems along with a liquid metal droplet injector to prepare samples *in-vacuo* for plasma exposures provides a broad spectrum of material characterization for a variety of different samples. As HIDRA-MAT continues to be developed, it will evolve into the primary material characterization device for samples that require *in-vacuo* characterization after long-pulse plasma exposures.

The sample preparation systems accommodate different sample needs that each experiment requires. Sample exposures can be performed at the plasma edge or into the core. Rotation of the sample can place the same at specific angles with respect to plasma to study AOI effects or how different plasma shapes lead to particle transport change. Unique to HIDRA-MAT compared to other characterization devices on fusion research machines is the ability to apply liquid metals to samples and expose them to plasmas *in-vacuo.* In particular, lithium's high reactivity in the air makes it unfavorable to transfer into atmosphere after plasma exposure for characterization. HIDRA-MAT's diagnostic capabilities allow it to unveil new information on the PMI mechanism by eliminating passivation effects that typically accompany the sample's characterization in atmosphere.

LIBS and TDS represent the two main characterization diagnostics on HIDRA-MAT. LIBS is considered a minimally destructive technique and TDS a destructive one. Together LIBS and TDS can be utilized to understand the surface PMI of exposed samples. LIBS can even be used in

between exposures to gain a temporal evolution of the surface, further understanding the dominant PMI mechanisms. Aside from the main characterization techniques, specific tools can be used on HIDRA-MAT if required. The sample heater used in TDS can be used to expose samples at different temperatures. The dual-RGA system can be operated in tandem with TDS to differentiate between deuterium and helium with a ±5% error. Also, an RGA can be moved to the main chamber to perform LIDS during LIBS in some cases. Overall, a large amount of information can be collected in HIDRA-MAT without leaving vacuum, thus enabling HIDRA-MAT to gather data in an environment that is more representative of the environments PFCs will encounter.

Future experiments on HIDRA-MAT will understand the behavior of liquid metal PFCs in HIDRA's stellarator plasmas. Lithium's beneficial properties have brought it to the forefront of next-generation PFC design and development in the fusion community. HIDRA-MAT's design accommodates the unique challenges associated with liquid metals. It can provide crucial fundamental information about liquid metal-material-plasma interfaces that are much needed to develop next-generation PFCs. The preliminary results demonstrating HIDRA-MAT's functionality via sample preparation, plasma exposure, LIBS, LIDS, TDS, and He/D_2 differentiation outline the vast potential HIDRA-MAT holds in the area of material science and specifically fusion PFC research.

Appendix A: Raman Spectroscopy

A.1 Background

Raman spectroscopy is a fast, non-destructive characterization technique that uses monochromatic light to gain molecular bond information from the sample surface's first few nanometers [37]. Photons interact with the molecular bonds, and through bond vibrations, polarization of the photon can occur. The most common interaction is Rayleigh scattering, where a photon excites an electron, and the electron then falls back to its ground state, emitting a photon with the same energy as the incident one. Less common are the Stokes lines that produce Raman spectra. This inelastic process occurs when an electron is excited and then de-excites to a vibrational state instead of its ground state, thus the emitted photon has less energy than the incident one. The spectrum created from the energy of the emitted light is known as the Raman shift. Molecules are identified by their Raman shifts by matching peaks in the recorded spectrum to known peaks for molecules. More than 99% of the scattered light experiences no shift, so the beam intensity must be large enough to produce a signal. Different wavelengths of light produce different Raman spectra. Raman can also be done on solids and liquids. Gases are difficult due to the low density of photon-bond interaction.

The formation of lithium deuteride has been of interest in the HIDRA-MAT project, and Raman was identified as a potential characterization technique to gain qualitative data on deuterium retention in liquid metals. Work at UIUC has investigated lithium hydride and lithium deuteride formation and developed ways to separate the hydrogen from the lithium as a proof of concept for a liquid metal loop system [38]. The behavior trends of lithium and hydrogen seen in these experiments can be applied to understanding the retention behavior of PFCs that have had liquid lithium applied to them. Raman's poor characterization of gases and metals stood out as

potential issues. However, because of lithium's high affinity for capturing hydrogen, there was a possibility that the density of bonds could become significant enough to be seen by Raman. Hypothesizing that, along with Raman's non-destructive properties, made this a viable option to explore.

Lithium hydride has been identified in crystals using Raman, and other Raman experiments show that the oxidation of lithium is exceptionally prevalent. Lithium's reactive nature subjects it to quick oxidation of the surface, and this occurs at a rate of one monolayer of impurities per second at 10^{-6} Torr [36]. In atmosphere, the surface is oxidized immediately since the amount of time it takes for the monolayer formation decreased linearly with an increase in magnitude of the pressure. Table 2 and figure 38 show the oxides' Raman shifts formed when lithium is present [39]. LiD Raman peaks have only been collected through crystals, and the main peak is at 328 cm^{-1} [40]. To mitigate the effect oxide formation has on the surface, the sample needs to be in vacuum during testing. Furthermore, before in-vacuum testing with a specialized Raman system could be done, it needed to be seen if the results seen in the papers could be reproduced with tungsten substrates.

Table 2. List of common Raman peak positions for lithium oxides in air *[39]*.

	Peak Position cm^{-1}	Symmetry	Reference	Peak Position (this work) cm^{-1}
$LiOH{\cdot}H_2O$, H_20- -Asym. stretch -Sym. stretch -Rock	**2626** **2813** 839	*Bg* *Ag* *Bg*	ii	2379, 2790, 2958 (LiOH) **2803 (Li_2O_2)**
LiOH, OH−stretch OH lib	3455 696	*Ag*	ii	192,141, 285, 294(3), 324(1), 514, 617, 1085(2)
Li_3N	538 605 689	2TA E_{2g} 2TO	iii	389, 452,576, **3090**
Li_2O	523	F_{2g}	i	525
Li_2C_2	1845	C≡C	i	
Li_2CO_3	866, 880 1441	TO LO TO	i	123,154,191,1089,1459,1713,1785
Li_2O_2	954 741 639	A_g A'_g B_{1g}	iv	129(3), 254(2), 786(1), **2803**

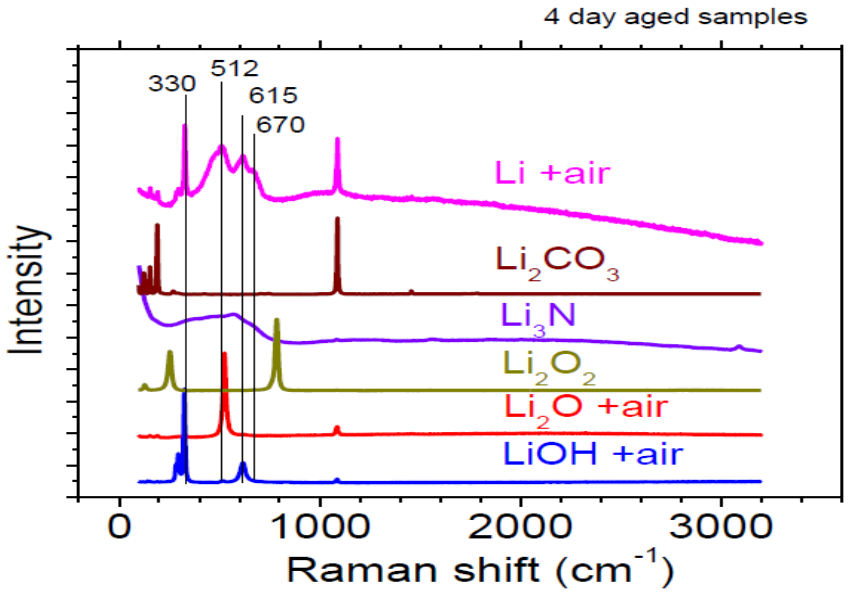

Figure 38. Comparison of lithium oxides' Raman spectra *[39]*.

A.2 Experimental Setup

Before a design for the Raman system on HIDRA-MAT could be finalized, there needed to be evidence that lithium deuteride could be identified through Raman on samples comparable to those in HIDRA-MAT. The Material Research Lab at UIUC hosts a Nanophoton Raman 11 system equipped with 532 nm and 785 nm wavelengths. Specific wavelengths of light produce Raman shifts that are more intense and easier to identify than the background spectrum. This Raman system operates in atmosphere so that any lithiated sample would be oxidized. Oxidation of a sample *in-vacuo* is expected in HIDRA-MAT over time. If the MRL Raman system could identify the lithium oxides, it would be likely that the HIDRA-MAT setup could also identify these bonds. Moreover, if lithium deuteride bonds were seen, then there would be clear evidence supporting the use of a Raman system on HIDRA-MAT.

Sample preparation started with collecting control data on bare samples to compare the Raman spectrum to literature. Following the control data acquisition, spectrum samples were to be lithiated, irradiated with deuterium, and lithiated then irradiated with deuterium. A total of 12 samples were prepared for Raman characterization, including silicon, tungsten, and porous tungsten. Silicon was used because it is used mainly in Raman applications and provides a strong Raman signal. If lithium oxides were not identifiable on a silicon substrate, Raman would have to be replaced with another characterization technique.

Samples ranged in size and shape and were lithiated using lithium evaporation in MCATS at CPMI. It is estimated based on the evaporation time that 50-100 nm of lithium was deposited on the sample surface. After lithiation, the samples that required irradiation were then moved to IGNIS in MRL. Due to availability on IGNIS, only four samples were irradiated, which included bare silicon, lithiated silicon, bare tungsten, and tungsten with lithium. The samples were irradiated

with deuterium at a fluence of 10^{19} cm^{-2} for 24.6 minutes leading to a flux of 6.7×10^{15} cm^2 s^{-1}. After irradiation, samples were stored until Raman was able to be done.

Raman testing was conducted and completed within six days of irradiation. The lithiated samples' surfaces passivated between the time of lithiation and irradiation but did not affect the tests' integrity since the interest was to identify lithium oxides in the Raman spectra. A laser with a wavelength of 532 nm and 50 mW of power was used for each sample, with the only difference between sample spectra being the used grating.

A.3 Experimental Results and Conclusions

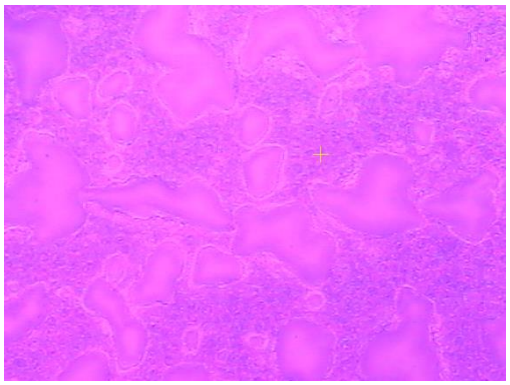

Figure 39. Raman image of lithiated Si sample.

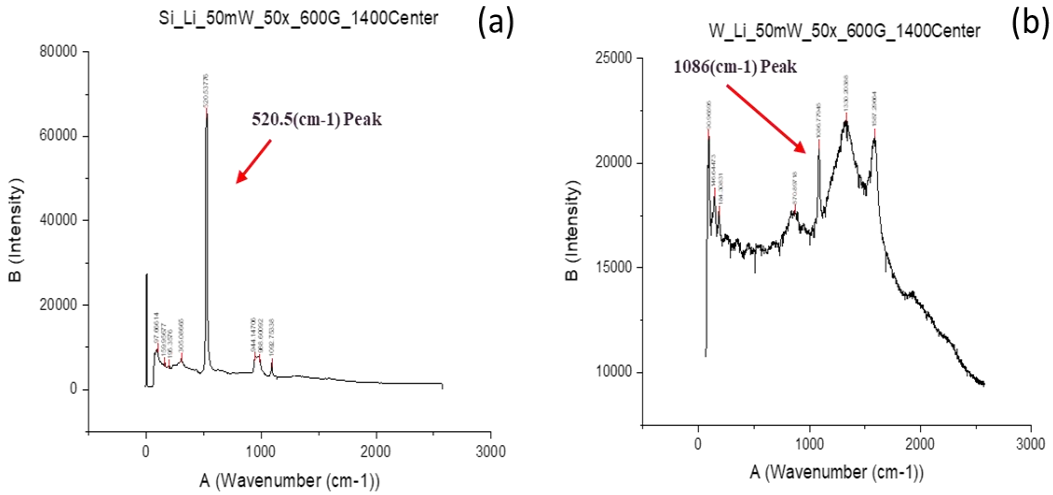

Figure 40. Raman spectra of (a) a lithiated Si sample and (b) a lithiated W sample at 50 mW of power using a 532nm laser wavelength and 600 g/mm grating.

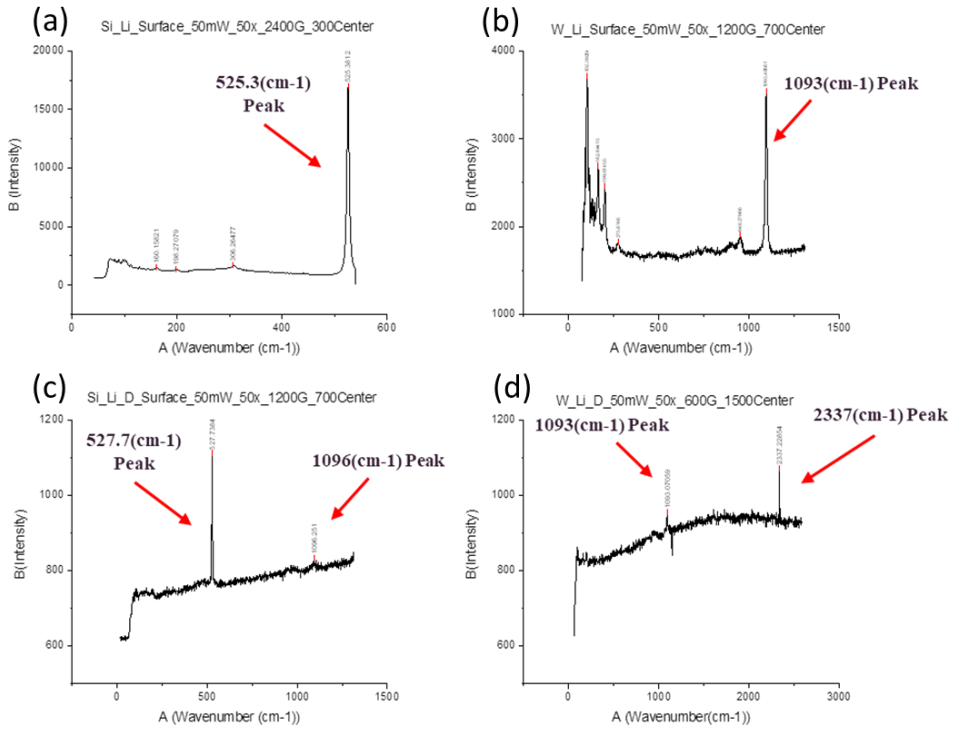

Figure 41. Raman spectra of a (a) lithiated Si sample, (b) lithiated W sample, (c) lithiated and deuterium irradiated Si sample, and (d) lithiated and deuterium irradiated W sample at 50 mW of power using a 532 nm laser wavelength and 1200 g/mm grating. The main Raman peaks observed are labeled; no significant conclusions could be made on if oxides were present.

Table 3. Raman Peak (cm^{-1}) wavenumbers for lithiated Si and W samples from figure 41.

Si_Li	W_Li	Si_Li_D	W_Li_D
160.1	102.3	527.7	1093
198.2	162.6	1096.2	2337.2
306.2	199.8		
525.3	275.6		
	948.2		
	1093.4		

The Raman spectra showed little to no conclusive evidence that a specialized *in-vacuo* HIDRA-MAT Raman system would identify lithium oxide or lithium deuteride bonds. Table 2 includes the prominent peaks seen for lithium oxides and lithium deuteride. Figure 39 is an image of the surface that was analyzed, and figures 40 and 41 show the Raman spectra of different samples with labeled peaks. To confidently conclude a bond is present, multiple peaks should be present in the Raman spectra. It became evident early on that the only peak consistently identifiable was the silicon peak. The lack of the known oxide peaks present on the spectra across each type of sample was reason enough to conclude that Raman was not a suitable characterization option. The adaptation from the MRL Raman system to HIDRA-MAT would have required considerable simplification, and no justification can be given to dedicating the time and resources in this project to exploring this technique for *in-vacuo* characterization further.

Appendix B: He/D_2 Differentiation Error Propagation Data

Table 4. Different combinations of flow rates were used for each mixture type. Data correspond to figures 26 and 27.

25 He : 75 D_2		**50 He : 50 D_2**		**75 He : 25 D_2**	
He Flow (sccm)	D_2 Flow (sccm)	He Flow (sccm)	D_2 Flow (sccm)	He Flow (sccm)	D_2 Flow (sccm)
2.3	2	3.73	3	3	2.03
2.73	3	5	4	4	2.29
3.15	4	6.29	5	5	2.55
3.58	5	7.57	6	6	2.81
4	6	8.85	7	7	3.07
4.43	7	10.13	8	8	3.33
4.86	8	11.41	9	9	3.59
5.29	9				

Table 5. Term contributions in the standard deviation calculation for the He percentage calculation. Results show the error in the calculation is mostly from the He pressure term.

25 He : 75 D_2		**50 He : 50 D_2**		**75 He : 25 D_2**	
$\left(\frac{\partial f}{\partial P_{He}}\right)^2 (\Delta P_{He})^2$	$\left(\frac{\partial f}{\partial P_{D_2}}\right)^2 (\Delta P_{D_2})^2$	$\left(\frac{\partial f}{\partial P_{He}}\right)^2 (\Delta P_{He})^2$	$\left(\frac{\partial f}{\partial P_{D_2}}\right)^2 (\Delta P_{D_2})^2$	$\left(\frac{\partial f}{\partial P_{He}}\right)^2 (\Delta P_{He})^2$	$\left(\frac{\partial f}{\partial P_{D_2}}\right)^2 (\Delta P_{D_2})^2$
189.62	0.10043	6.715	0.047197	13.787	0.17601
37.951	0.021867	6.0965	0.030383	2.8166	0.077952
31.278	0.010628	4.6279	0.021047	1.2465	0.054821
18.369	0.010792	2.8756	0.018707	0.71827	0.035401
20.845	0.010333	2.8812	0.014241	0.55843	0.020968
18.42	0.011099	3.9881	0.011524	0.51721	0.020847
15.756	0.0060471	4.8333	0.011836	0.51831	0.015075
18.666	0.0068327				

Table 6. Term contributions in the standard deviation calculation for the D_2 pressure calculation. Results show the error in the calculation is mostly from the measurement of the 25 eV signal.

25 He : 75 D_2		**50 He : 50 D_2**		**75 He : 25 D_2**	
$\left(\frac{\partial P_{D_2}}{\partial m}\right)^2 (\Delta m)^2$	$\left(\frac{\partial P_{D_2}}{\partial x}\right)^2 (\Delta x)^2$	$\left(\frac{\partial P_{D_2}}{\partial m}\right)^2 (\Delta m)^2$	$\left(\frac{\partial P_{D_2}}{\partial x}\right)^2 (\Delta x)^2$	$\left(\frac{\partial P_{D_2}}{\partial m}\right)^2 (\Delta m)^2$	$\left(\frac{\partial P_{D_2}}{\partial x}\right)^2 (\Delta x)^2$
1.50E-40	5.64E-12	3.45E-40	9.40E-12	1.62E-40	4.05E-12
3.45E-40	9.20E-12	6.4E-40	1.90E-11	2.08E-40	5.24E-12
6.15E-40	1.47E-11	1.09E-39	2.94E-11	2.68E-40	8.33E-12
1.01E-39	2.42E-11	1.68E-39	4.75E-11	3.33E-40	9.87E-12
1.58E-39	4.65E-11	2.50E-39	6.20E-11	4.15E-40	9.24E-12
2.30E-39	7.17E-11	3.80E-39	8.06E-11	4.98E-40	1.36E-12
3.24E-39	6.03E-11	5.44E-39	1.27E-11	6.12E-40	1.37E-12
4.37E-39	1.09E-11				

Table 7. Standard deviations associated with the RGA signal measurements. Standard deviation does change with each different combination of He and D_2 flow rates.

25 He : 75 D_2		**50 He : 50 D_2**		**75 He : 25 D_2**	
25 eV Measurement SD (Δx)	50 eV Measurement SD (Δw)	25 eV Measurement SD (Δx)	50 eV Measurement SD (Δw)	25 eV Measurement SD (Δx)	50 eV Measurement SD (Δw)
1.86249E-9	1.38413E-8	2.40368E-9	2.49378E-8	1.5784E-9	1.63707E-8
2.37736E-9	2.49636E-8	3.42174E-9	3.42287E-8	1.79459E-9	1.9561E-8
3.00908E-9	3.6159E-8	4.25229E-9	4.99414E-8	2.26308E-9	2.10694E-8
3.86358E-9	3.65117E-8	5.40449E-9	5.89786E-8	2.46331E-9	2.41716E-8
5.34585E-9	5.42978E-8	6.1749E-9	5.97963E-8	2.38356E-9	2.6419E-8
6.63986E-9	6.98446E-8	7.03879E-9	7.43155E-8	2.89749E-9	3.54362E-8
6.09035E-9	7.23007E-8	8.83442E-9	1.06809E-7	2.90493E-9	4.14944E-8
8.1956E-9	9.24723E-8				

Table 8. Term contributions in the standard deviation calculation for the He pressure calculation. Results show the error in the calculation is mostly from the calculation of the 50 eV He pressure calculation. With higher concentrations of He, the term contribution becomes more even but still is due to the 50 eV He pressure calculation.

25 He : 75 D_2		**50 He : 50 D_2**		**75 He : 25 D_2**	
$\left(\frac{\partial P_{He}}{\partial l}\right)^2 (\Delta l)^2$	$\left(\frac{\partial P_{He}}{\partial z}\right)^2 (\Delta z)^2$	$\left(\frac{\partial P_{He}}{\partial l}\right)^2 (\Delta l)^2$	$\left(\frac{\partial P_{He}}{\partial z}\right)^2 (\Delta z)^2$	$\left(\frac{\partial P_{He}}{\partial l}\right)^2 (\Delta l)^2$	$\left(\frac{\partial P_{He}}{\partial z}\right)^2 (\Delta z)^2$
9.82E-12	3.70E-10	2.67E-11	1.24E-09	1.50E-11	4.09E-10
1.31E-11	1.23E-09	4.14E-11	2.88E-09	2.68E-11	6.16E-10
1.58E-11	2.80E-09	7.53E-11	5.96E-09	4.45E-11	8.75E-10
2.34E-11	4.44E-09	1.46E-10	9.65E-09	7.01E-11	1.19E-09
2.82E-11	8.72E-09	1.94E-10	1.38E-08	9.60E-11	1.49E-09
4.01E-11	1.41E-08	2.10E-10	2.14E-08	1.34E-10	2.37E-09
4.96E-11	1.81E-08	2.68E-10	3.54E-08	1.68E-10	3.14E-09
5.36E-11	2.75E-08				

Table 9. Term contributions in the standard deviation calculation for the He pressure calculation. Results show relatively equal error contribution from the measured 50 eV RGA signal and the calculated 50 eV D_2 signal.

25 He : 75 D_2		**50 He : 50 D_2**		**75 He : 25 D_2**	
50 eV Measurement SD $(\Delta w)^2$	50 eV D_2 Signal SD $(\Delta y)^2$	50 eV Measurement SD $(\Delta w)^2$	50 eV D_2 Signal SD $(\Delta y)^2$	50 eV Measurement SD $(\Delta w)^2$	50 eV D_2 Signal SD $(\Delta y)^2$
1.92E-16	2.09E-16	6.22E-16	7.24E-16	2.68E-16	1.75E-16
6.23E-16	7.11E-16	1.17E-15	1.94E-15	3.83E-16	2.83E-16
1.31E-15	1.72E-15	2.49E-15	3.95E-15	4.44E-16	5.01E-16
1.33E-15	3.47E-15	3.48E-15	6.95E-15	5.84E-16	7.08E-16
2.95E-15	6.48E-15	3.58E-15	1.14E-14	6.98E-16	9.17E-16
4.88E-15	1.04E-14	5.52E-15	1.76E-14	1.26E-15	1.30E-15
5.23E-15	1.43E-14	1.14E-14	2.69E-14	1.72E-15	1.68E-15
8.55E-15	2.12E-14				

Table 10. Term contributions in the standard deviation calculation for the 50 eV D_2 signal calculation. Results show that the error is contributed by the D_2 pressure term. Referring back to table 6, the error comes from the measurement of the 25 eV RGA signal.

25 He : 75 D_2		**50 He : 50 D_2**		**75 He : 25 D_2**	
$\left(\frac{\partial y}{\partial n}\right)^2 (\Delta n)^2$	$\left(\frac{\partial y}{\partial P_{D_2}}\right)^2 \left(\Delta P_{D_2}\right)^2$	$\left(\frac{\partial y}{\partial n}\right)^2 (\Delta n)^2$	$\left(\frac{\partial y}{\partial P_{D_2}}\right)^2 \left(\Delta P_{D_2}\right)^2$	$\left(\frac{\partial y}{\partial n}\right)^2 (\Delta n)^2$	$\left(\frac{\partial y}{\partial P_{D_2}}\right)^2 \left(\Delta P_{D_2}\right)^2$
3.50E-17	0.10043	4.34E-16	0.047197	4.96E-17	0.17601
4.27E-16	0.021867	1.35E-15	0.030383	1.21E-16	0.077952
1.26E-15	0.010628	3.04E-15	0.021047	2.44E-16	0.054821
2.72E-15	0.010792	5.48E-15	0.018707	4.03E-16	0.035401
5.04E-15	0.010333	9.48E-15	0.014241	6.31E-16	0.020968
8.21E-15	0.011099	1.51E-14	0.011524	8.83E-16	0.020847
1.24E-14	0.0060471	2.29E-14	0.011836	1.25E-15	0.015075
1.78E-14	0.0068327				

References

[1] J. Team, "FUSION ENERGY PRODUCTION FROM A DEUTERIUM-TRITIUM PLASMA IN THE JET TOKAMAK," *Nucl. Fusion*, vol. 32, no. 2, pp. 187-203, 1992.

[2] R. Rizkallah, D. Andruczyk, A. Shone and et al., "Latest Results From the Hybrid Illinois Device for Research and Applications (HIDRA)," *IEEE Trans. Plasma Sci.*, vol. 46, no. 7, pp. 2685-2690, 2018.

[3] S. Marcinko and D. Curreli, "Numerical characterization of the edge transport conditions and limiter fluxes of the HIDRA stellarator," *Phys. Plasmas*, vol. 25, p. 022507, 2018.

[4] P. Fiflis, N. Connolly and D. Ruzic, "Experimental mechanistic investigation of the nanostructuring of tungsten with low energy helium plasmas," *J. Nucl. Mater.*, vol. 482, pp. 201-209, 2016.

[5] D. Liu, S. Dai, M. Wada and e. al., " Modelling of hydrogen reflection on tungsten fuzzy surface in an erosive hydrogen plasma," *Nucl. Fusion*, vol. 60, p. 056018, 2020.

[6] Z. S. Hartwig, H. S. Barnard, B. N. Sorbom and e. al., "Fuel Retention Measurements in Alcator C-Mod using accelerator-based in situ material surveillance," *J. Nucl. Mater.*, vol. 463, p. 73–77, 2015.

[7] D. Ruzic, W. Xu, D. Andruczyk and e. al., " Lithium–metal infused trenches (LiMIT) for heat removal in fusion devices," *Nucl. Fusion*, vol. 51, p. 102002, 2011.

[8] D. Andruczyk, R. Maingi, J. Hu and e. al., "Overview of lithium injection and flowing liquid lithium results from the US–China collaboration on EAST," *Phys. Scr.* , vol. T171, p. 014067, 2020.

[9] D. Ruzic, M. Szott, C. Sandoval and e. al., "Flowing liquid lithium plasma-facing components - Physics, technology and system analysis of the LiMIT system," *Nucl. Mater. Energy*, no. 12, pp. 1324-1329, 2017.

[10] C. Taylor, B. Heim, S. Gonderman and e. al., "Materials analysis and particle probe: A compact diagnostic system for in situ analysis of plasma-facing components.," *Rev. Sci. Instrum.*, vol. 83, p. 10D703, 2012.

[11] P. Fiflis, A. Press, W. Xu and e. al., "Wetting properties of liquid lithium on select fusion relevant surfaces," *Fusion Eng. Des.*, vol. 89, pp. 2827-2832, 2014.

[12] M. Zibrov, Y. Gasparyan, S. Ryabtsev and e. al., " Isolation of peaks in TDS spectra of deuterium from ion irradiated tungsten," *Phys. Procedia*, vol. 71, pp. 83-87, 2015.

[13] R. Rizkallah, S. Marcinko, D. Curreli and e. al., "Mapping of the HIDRA stellarator magnetic flux surfaces," *Phys. Plasmas*, vol. 26, p. 092503, 2019.

[14] R. Maingi, R. Majeski, J. E. Menard and e. al., "Lithium as a plasma facing component to optimize the edge plasma," in *IEEE 26th Symposium on Fusion Engineering*, Austin, TX, 2015.

[15] A. L. Roquemore, D. Andruczyk, R. Majeski and e. al., "Upward-facing lithium flash evaporator for NSTX-U," in *IEEE 25th Symposium on Fusion Engineering (SOFE)*, San Francisco, CA, 2013.

[16] A. Nagy, A. Bortolon, E. P. Gilson and e. al., " Lithium granular injector operational experience triggering ELMs in H-mode on DIII-D," in *IEEE 26th Symposium on Fusion Engineering (SOFE)*, Austin, TX, 2015.

[17] D. Mansfield, A. Roquemore, H. Schneider and e. al., "A simple apparatus for the injection of lithium aerosol into the scrape-off layer of fusion research devices," *Fusion Eng. Des.*, vol. 85, pp. 890-895, 2010.

[18] M. J. Baldwin, T. Lynch, L. Chousal and e. al., "An injector device for producing clean-surface liquid metal samples of Li, Ga and Sn–Li in vacuum," *Fusion Eng. Des.*, vol. 70, no. 2, pp. 107-113, 2004.

[19] V. K. Alimov and B. Scherzer, "Deuterium retention and re-emission from tungsten materials," *J. Nucl. Mater.*, vol. 240, pp. 75-80, 1996.

[20] X. Jiang, G. Sergienko and B. Schweer, "An upgraded LIBS system on linear plasma device PSI-2 for in situ diagnostics of plasma-facing materials," *Fusion Eng. Des.*, vol. 146, pp. 96-99, 2019.

[21] M. Christenson, D. Panici and C. Moynihan, "A study on hydrogen absorption and dissolution in liquid lithium," *Nucl. Fusion* , vol. 59, no. 2, 2019.

[22] M. Christenson, C. Moynihan and D. Ruzic, "A distillation column for hydrogen isotope removal from liquid lithium," *Fusion Eng. and Des.*, vol. 135, pp. 81-87, 2018.

[23] D. Dasgupt, R. D. Kolasinski, R. W. Friddle and e. al., "On the origin of ‘fuzz’ formation in plasma-facing," *Nucl. Fusion,* vol. 59, p. 086057, 2019.

[24] Y. Yu, J. Hu, Z. Wan and e. al., "Mass separation of deuterium and helium with conventional quadrupole mass spectrometer by using varied ionization energy," *Rev. Sci. Instrum.* , vol. 87, p. 035120, 2016.

[25] F. Anabitarte, A. Cobo and J. M. Lopez-Higuera, "Laser-Induced Breakdown Spectroscopy: Fundamentals, Applications, and Challenges," *ISRN Spec.*, vol. 2012, p. 285240, 2012.

[26] C. Li., D. Zhao and X. Wu, "Spatial Resolution Measurements of C, Si and Mo Using LIBS for Diagnostics of Plasma Facing Materials in a Fusion Device*," *Plasma Sci. Tech.*, vol. 17, no. 8, pp. 638-643, 2015.

[27] J. Weiss, L. M. Cabalin and J. J. Laserna, "Angle of Observation Influence on Emission Signal from Spatially Confined Laser-Induced Plasmas," *Appl. Spec.*, vol. 7, no. 1, pp. 87-96, 2017.

[28] C. Li, X. Wu and C. Zhang, "Study of deuterium retention on lithiated tungsten exposed to high-flux deuterium plasma using laser-induced breakdown spectroscopy," *Fusion Eng. Des.*, vol. 89, pp. 949-954, 2014.

[29] H. Y. Oderji, N. Farid and L.Sun, "Evaluation of explosive sublimation as the mechanism of nanosecondlaser ablation of tungsten under vacuum conditions," *Spectochimica Acta Part B,* vol. 122, pp. 1-8, 2016.

[30] S. Almaviva, L. Caneve and F. Colao, "Double pulse Laser Induced Breakdown Spectroscopy measurementson ITER-like samples," *Fusion Eng. Des.,* Vols. 96-97, pp. 848-851, 2015.

[31] Z. Hu, C. Li, Q. Xiao and e. al., "Preliminary results of in situ laser-induced breakdown spectroscopy for the first wall diagnostics on EAST," *Plasma Sci. Technol.,* vol. 19, p. 025502, 2017.

[32] R. Hai, P. Liu, D. Wu and e. al., "Collinear double-pulse laser-induced breakdown spectroscopy as an in-situ diagnostic tool for wall composition in fusion devices," *Fusion Eng. Des.,* vol. 89, pp. 2435-2439, 2014.

[33] D. Zhao, N. Farid, R. Hai and e. al., "Diagnostics of First Wall Materials in a Magnetically Confined Fusion Device by Polarization-Resolved Laser-Indiced Breakdown Spectroscopy," *Plasma Sci. Technol.,* vol. 16, pp. 149-154, 2014.

[34] L. Mercadier, J. Hermann, C. Grisolia and e. al., "Plume segregation observed in hydrogen and deuterium containing plasmasproduced by laser ablation of carbonfiber tiles from a fusion reactor," *Spectrochimica Acta Part B,* vol. 65, pp. 715-720, 2010.

[35] X. Jiang, G. Sergienko, B. Schweer and e. al., "An upgraded LIBS system on linear plasma device PSI-2 for in situdiagnostics of plasma-facing materials," *Fusion Eng. Des.,* vol. 146, pp. 96-99, 2019.

[36] D. Alpert, " New Developments in the Production and Measurement of Ultra High Vacuum," *J. Applied Phys.* , vol. 24, p. 860, 1953.

[37] C. RAMAN and K. KRISHNAN, "A New Type of Secondary Radiation," *Nature,* vol. 121, pp. 501-502, 1928.

[38] M. Christenson, C. Moynihan and D. N. Ruzic, "A distillation column for hydrogen isotope removal from liquid lithium," *Fusion Eng. Des.,* vol. 135, pp. 81-87, 2018.

[39] A. Kumar, T. M. Arruda., A. Tselev and e. al., "Nanometer-scale mapping of irreversible electrochemical nucleation processes on solid Li-ion electrolytes," *Sci. Reports,* vol. 3, p. 1621, 2013.

[40] V. S. Gorelik, B. Dongxue, Y. P. Voinov and e. al., "Raman spectra of lithium compounds," *J. Phys.: Conf. Ser.,* vol. 918, p. 012035, 2017.

[41] J. Scaffidi, S. M. Angel and D. A. Cremers, "Analytical Chemistry," *Enhancement Mechanisms in Dual-Pulse LIBS,* pp. 25-32, 1 January 2006.